

Structural characteristics of shallow faults in the Delaware Basin

Elizabeth A. Horne¹, Peter H. Hennings¹, Katie M. Smye¹, Scott Staniewicz², Jingyi Chen², and Alexandros Savvaidis¹

Abstract

The Delaware Basin of Texas and New Mexico is experiencing elevated levels of seismicity. There have been more than 130 earthquakes with local magnitudes of at least 3.0 recorded between 2017 and 2021, with earthquakes occurring in spatiotemporally isolated and diffuse clusters. Many of these events have been linked to oilfield operations such as hydraulic fracturing and wastewater disposal at multiple subsurface levels; however, the identification and characterization of earthquake-hosting faults have remained elusive. There are two distinct levels of faulting in the central region of the basin where most earthquakes have been measured. These fault systems include a contractional basement-rooted fault system and a shallow extensional fault system. Shallow faults trend parallel to and rotate along with, the azimuth of S_{HMAX} , are vertically decoupled from the basement-rooted faults, accommodate dominantly dip-slip motion, and are the product of more recent processes including regional exhumation and anthropogenic influences. The shallow fault system is composed of northwest–southeast-striking, high angle, and parallel trending faults which delineate a series of elongate, narrow, and extensional graben. Although most apparent in 3D seismic reflection data, these narrow elongate graben features also are observed from interferometric synthetic aperture radar (InSAR) surface deformation measurements and can be delineated using well-located earthquakes. In contrast to the basin-compartmentalizing basement-rooted fault system, shallow faults do not display any shear movement indicators, and they have small throw displacement given their mapped length, producing an anomalous mean throw-to-length ratio of 1:1000. These characteristics indicate that these features are more segmented than can be mapped with conventional subsurface data. Much of the recent seismicity in the south-central Delaware Basin is associated with these faults and InSAR surface deformation observations find that these faults also may be slipping aseismically.

Introduction

The Permian Basin of West Texas and southeast New Mexico is a prolific petroleum-producing region approximately 480 km long and 400 km wide and accounts for more than 39 billion barrels of oil and 138 trillion cubic feet of natural gas production from conventional and unconventional reservoirs at multiple subsurface levels (Energy Information Administration [EIA], 2018, 2020, 2021). Unconventional development of hydrocarbons through horizontal drilling and hydraulic fracturing (HF) has occurred over the past 10 years, targeting primarily Wolfcampian and Leonardian-age strata. More than 17,000 horizontal wells have been drilled in the basin, with a peak of nearly 3000 wells/year drilled in 2018–2019. This unconventional development also has resulted in significant volumes of HF flowback and produced formation water. The primary target for saltwater disposal (SWD) of these volumes in the central

Delaware Basin is in shallow, depleted conventional reservoirs of the late Permian, Guadalupian-age Delaware Mountain group (DMG) (Smye et al., 2021a). These formations received more than 11 billion barrels of cumulative disposal from 2010 to 2021, with annual disposal volumes peaking at 1.7 billion barrels in 2018 (Smye et al., 2021a).

This region also has experienced an increased number of earthquakes with local magnitudes (M_L) ≥ 3.0 beginning in 2009 with the rate of seismicity accelerating from 2016 to 2021 (Ellsworth, 2013; Lomax and Savvaidis, 2019; Savvaidis et al., 2019; Frohlich et al., 2016, 2020). Since the implementation of the Texas Seismological Network (TexNet) (Savvaidis et al., 2019), the Delaware Basin has hosted more than 1100 earthquakes of $M_L 2.5+$, 4000 earthquakes of $M_L 2.0+$, and 9400 $M_L 1.5+$ from 2017 to 2021 (TexNet Earthquake Catalog, 2022).

¹The University of Texas at Austin, Bureau of Economic Geology, Austin, Texas, USA. E-mail: lily.horne@beg.utexas.edu (corresponding author); peter.hennings@beg.utexas.edu; Katie.smye@beg.utexas.edu; alexandros.savvaidis@beg.utexas.edu.

²The University of Texas at Austin, Department of Aerospace Engineering and Engineering Mechanics, Austin, Texas, USA. E-mail: scott.staniewicz@utexas.edu; jingyi.ann.chen@utexas.edu.

Manuscript received by the Editor 21 January 2022; revised manuscript received 11 May 2022; published ahead of production 9 August 2022; published online 27 September 2022. This paper appears in *Interpretation*, Vol. 10, No. 4 (November 2022); p. T807–T835, 17 FIGS., 4 TABLES. <http://dx.doi.org/10.1190/INT-2022-0005.1>. © 2022 Society of Exploration Geophysicists and American Association of Petroleum Geologists

Previous work on these earthquake sequences has shown that earthquakes in the northern Delaware Basin are associated with deep SWD (Lomax and Savvaidis, 2019; Savvaidis et al., 2020; Skoumal et al., 2020; Tung et al., 2020; Grigoratos et al., 2022) whereas, in the study area of the southern Delaware Basin, earthquakes are associated with shallow SWD and HF (Grigoratos et al., 2022). Earthquake clusters that are spatiotemporally isolated are more likely to be related to HF, however, but previous work completed by Grigoratos et al. (2022) has determined that most of the earthquake sequences in the southcentral Delaware Basin are associated with shallow SWD.

Geologic setting and paleostress architecture

The Permian Basin is a structured intracratonic basin, which has been shaped by several extensional

and compressional deformation events since the Proterozoic. These events have generated a well-defined network of regional faults whose footprints divide the Permian Basin spatially into several physiographic provinces, including the Delaware Basin, Midland Basin, and Central Basin platform (Figure 1).

The Permian Basin is tectonically varied and extends across several basement terranes, the southern crystalline area, the northern crystalline area, and the southern granite rhyolite province, and is generally Proterozoic in age (1000–1300 Ma) (Figures 2 and 3a; Flawn, 1956; Muehlberger, 1965; Muehlberger et al., 1967; Denison et al., 1971; Lund et al., 2015). The Proterozoic-age (approximately 1000 Ma) Grenville orogeny bisects the mapped region. Deformation and metamorphism from this northwest-verging orogenic event likely established a northeast–southwest-oriented crystalline grain, and

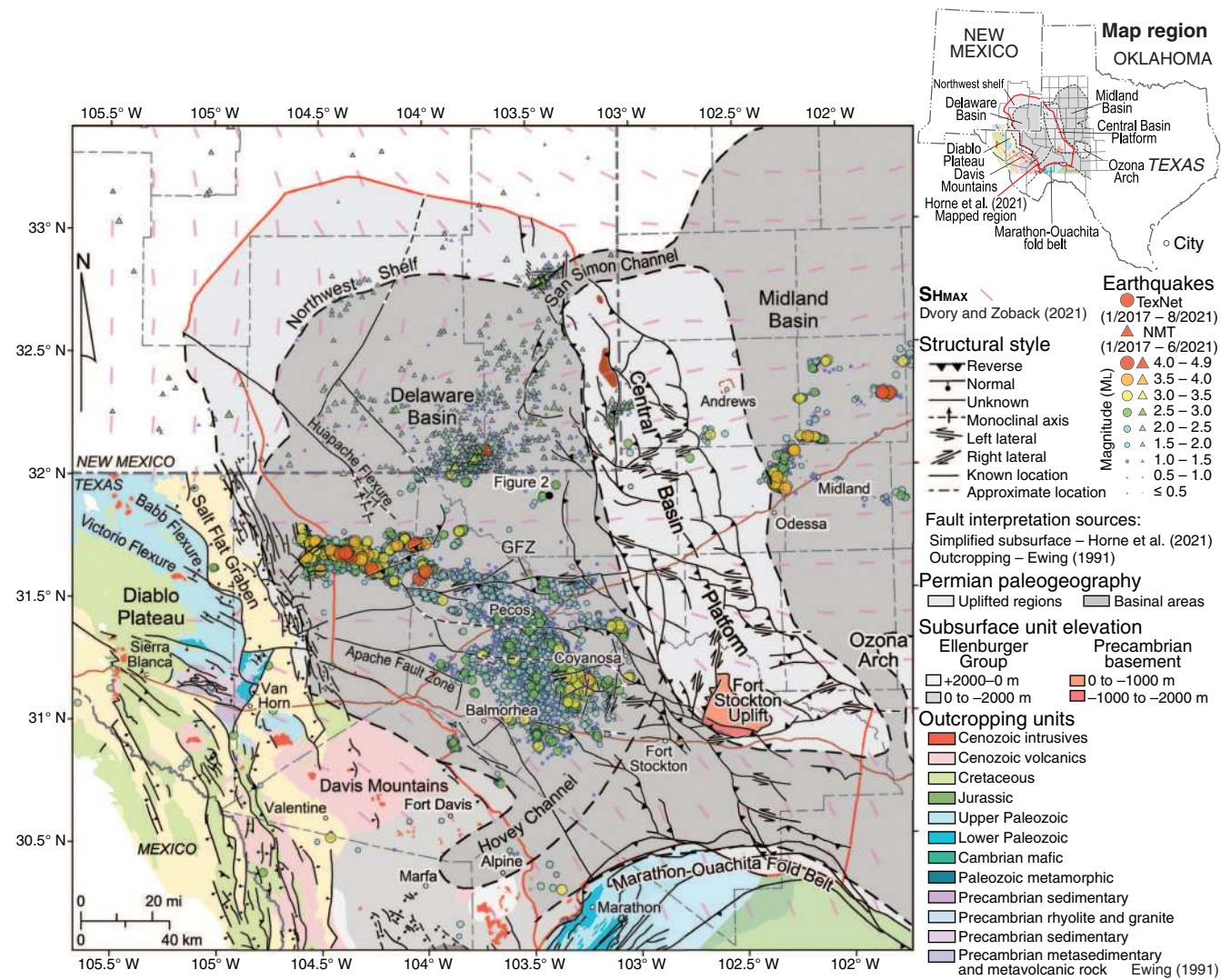


Figure 1. Generalized paleogeographic map of the western Permian Basin of West Texas and southeastern New Mexico. Permian depositional environments are labeled, and areal extents are shown in shades of gray. Principle subsurface basement-rooted faults are shown, and significant fault zones, flexures, and uplifts are labeled or abbreviated. GFZ, Grisham fault zone. Outcropping faults and stratigraphic units modified from Ewing (1991). Interpolated orientations of S_{HMAX} are shown (Dvory and Zoback, 2021). TexNet-located (Savvaidis et al., 2019) and New Mexico Tech Seismological Observatory-located earthquake hypocenters are shown as colored circles and triangles, respectively (last updated 30 August 2021). Modified after Horne et al. (2021).

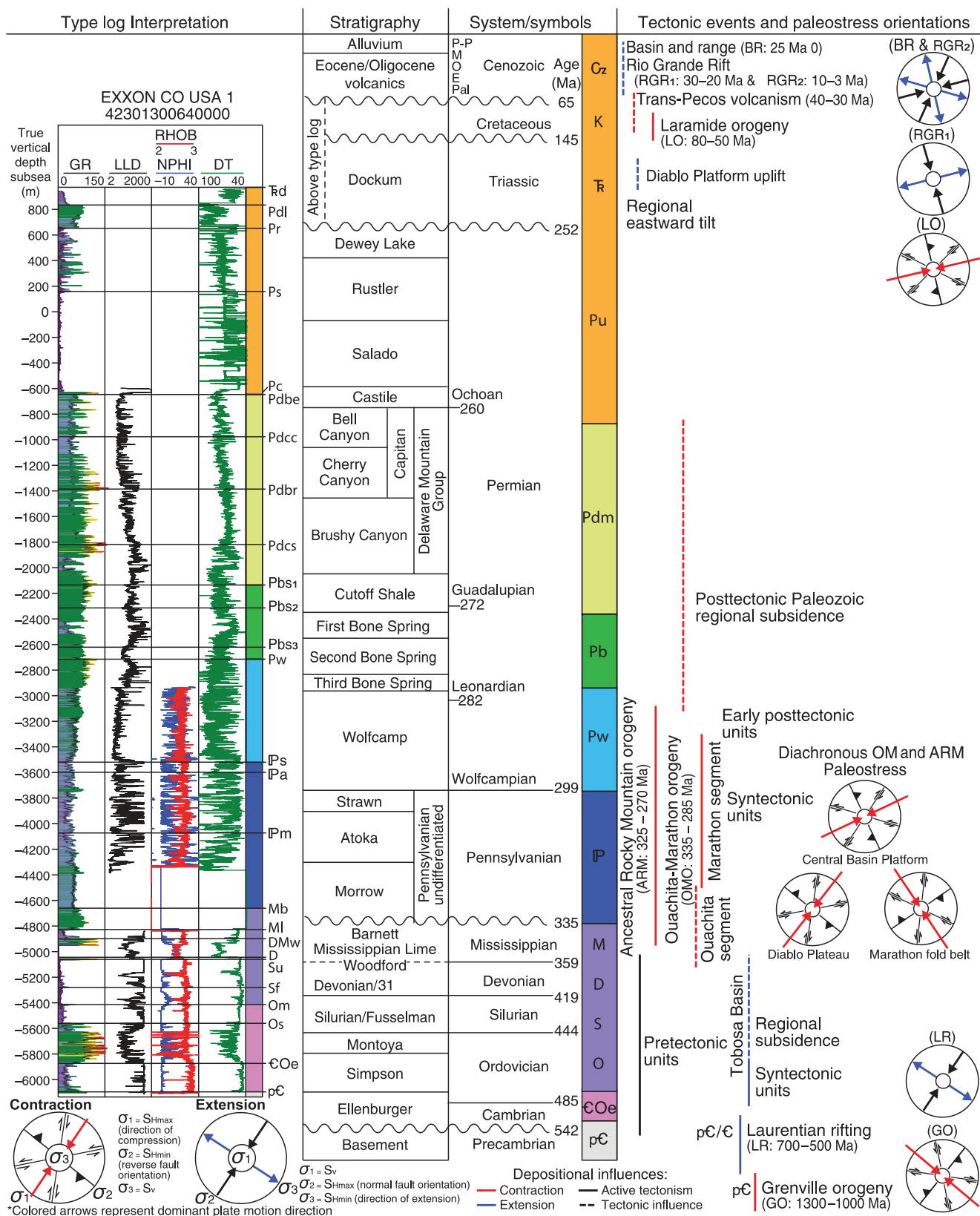


Figure 2. Type petrophysical log, stratigraphic units, and tectonic events impacting the western Permian Basin. Type-log well location is highlighted in Figure 1. Stratigraphy compiled in Ruppel (2019b), tectonic events, deformation directions, and depositional processes synthesized from Zoback and Zoback (1980), Horak (1985), Hentz and Henry (1989), Dickinson and Lawton (2003), Ewing (2015), Leary et al. (2017), Brown (2019), and Ruppel (2019b). Modified from Horne et al. (2021).

deformation from subsequent events were influenced by these fabrics through tectonic inheritance (Horak, 1985; Adams and Keller, 1996; Davis and Mosher, 2015). This crust was regionally exhumed, eroded flat (Rougvie et al., 1999; Ewing et al., 2019), and subsequent rifting initiated along the southern, northeast–southwest-trending Laurentian margin during the late Proterozoic (Horak, 1985; Ewing et al., 2019), which continued into the early Paleozoic (Walper, 1982). This continued northeast–southwest extension leads to the development of the Tobosa Basin, which is evidenced by depositional patterns and facies distributions of Cambrian-Silurian age strata (Figures 2 and 3b; Adams et al., 1951; Galley, 1958; Walper, 1977; Hills, 1984; Horak, 1985; Ross, 1986; Wuellner et al., 1986; Frenzel et al., 1988).

The principal tectonic elements that define the modern greater Permian Basin formed as a result of the diachronous collision between the northwest-verging Ancestral Rocky Mountain orogeny and northeast-verging Ouachita-Marathon orogeny (Figure 2; Dickinson and Lawton, 2003; Leary et al., 2017). Subsequent events are interpreted to have been influenced by the accumulated tectonic fabrics generated by these Paleozoic events; many of the structures exhibit characteristics of reactivation and transferred strain (Hills, 1970, 1984; Budnik, 1986; McConnell, 1989; Shumaker, 1992; Kluth, 1998). These events include the east-northeast-verging Laramide orogeny, (Hills, 1963; Henry et al., 1985; Hennings, 1994), basin-range extension, and the Rio Grande rifting (Figure 2; Henry and Price, 1986; Brown, 2019; Ruppel, 2019a). The post-Permian tectonic events control much of the modern landscape of the western Delaware Basin, and they have been attributed to heterogeneities in the principal stress orientation $S_{H\max}$ and current-day stresses of the southern Delaware Basin (Figures 1 and 2; Zoback and Zoback, 1980, 1989; Horak, 1985; Rickets et al., 2014; Lund Snee and Zoback, 2016, 2018, 2020; Dvory and Zoback, 2021).

The Delaware Basin contains more than 6000 m (approximately 20,000 ft) of preserved sediment fill. Early Paleozoic sedimentation consisted of passive-margin carbonates and shales, whereas fluvial-deltaic siliciclastic sediments and deepwater carbonates dominated after the structural differentiation of the basin (e.g., Ruppel, 2019a). Permian-age Wolfcampian and Leonardian age units targeted for horizontal drilling, including the Wolfcamp Formation and the Bone Spring group, consist of mixed carbonate-siliciclastic systems (Ruppel, 2019a; Fu et al., 2020; Fairhurst et al., 2021). The Guadalupian-age DMG overlying the Bone Spring group (Figure 3) is the target of shallow SWD and is dominated by clay-poor sandstones, generally accepted as turbidites deposited in the deepwater basin during relative sea-level lowstands (Silver and Todd, 1969; Gardner, 1992; Nance, 2020). Minor detrital carbonates were deposited proximal to carbonate platforms, and eolian siltstones reflecting transgressive-to-highstand conditions were deposited cyclically with coarser sandstones (Smee et al., 2021a). The varied lithology of the DMG is expected to result in

mechanical stratigraphy that may influence the nature of deformation in these units.

Previous work

Basement-rooted faults

Recent work by Horne et al. (2021) resulted in the generation of a new fault map and 3D faulted framework for basement-rooted faults of the Delaware Basin and Central Basin platform. An integrated subsurface data set of multiple 3D seismic reflection data sets, deep well penetrations, and interpretations provided by oil and gas operators enabled the identification of previously unmapped faults, as well as the amendment and validation of fault segments mapped from previous publications (Gardiner, 1990; Comer, 1991; Ewing, 1991; Shumaker, 1992; Yang and Dorobek, 1995; Tai and Dorobek, 2000). The data set, methodology, static structural characterization, and kinematic analysis of their interpretation are described in detail (Horne et al., 2021) and the process of converting 2D fault segments into 3D fault surfaces follows the methodology outlined in Hennings et al. (2019) and Horne et al. (2020).

Horne et al. (2021) identify three principal fault behaviors regionally, each with distinctive patterns, distributions, and interfault relationships that accompanied the Paleozoic Formation of the basin and its uplifted margins formation. Basement-involved deformation occurred along north-northwest–south-southeast-striking reverse faults, which initiated during Ancestral Rocky Mountain convergence and continued to evolve and lengthen throughout the overlapping Ancestral Rocky Mountain and Ouachita-Marathon orogenesis. Secondary, generally, east–west-striking faults compartmentalize the north-northwest–south-southeast-striking faults. These features are interpreted to be the product of the craton assembly during the Proterozoic time (former suture or transfer zones and metamorphic grains; Poole et al., 2005) that were reactivated under the combined tractions of the temporally overlapping Ancestral Rocky Mountain and Ouachita-Marathon orogenesis. Finally, north-northeast–south-southwest-striking faults are less developed and may have formed as linkages between north-northwest–south-southeast and east–west fault zones during the waning stages of Ancestral Rocky Mountain and Ouachita-Marathon orogenesis, or perhaps during a much later event, such as the Laramide orogeny.

Shallow faults

In an effort to understand trends in well performance and volumes of H_2S and water, previous researchers identified a set of subsurface features using a 3D seismic reflection data set. These attributes illuminated the presence of shallow, elongate, and narrow graben in Reeves Co., Texas. Charzynski et al. (2019) map and characterize these features and Cook et al. (2019) present a variety of geophysical calculations that enhance the seismic imagery. Although there is significant noise within the seismic stratigraphic units below the Leonardian age

(approximately 282–272 Ma) Bone Spring Formation (BSPG), seismic attribute interrelationship calculations generated by Cook et al. (2019) illuminated corridors of potential open-fracture networks within the Wolfcampian age (approximately 299–282 Ma) Wolfcamp interval. Work completed by Charzynski et al. (2019) and Cook et al. (2019) underscores the importance of obtaining and conducting seismic imaging-enhancement on 3D seismic reflection data sets to map and characterize these features, as these fault and open fracture zones have hindered oilfield operations by acting as conduits for vast volumes of H₂S and extraneous water production, rendering many wells uneconomic.

Fault slip potential

Recent work conducted by Hennings et al. (2021) leveraged new and previously mapped fault sets to investigate the link between elevated earthquake rates linked spatiotemporally to unconventional petroleum operations within the core seismogenic region of the Delaware Basin. Hennings et al. (2021) use basement-rooted faults that map and characterize by Horne et al. (2021), and compile a multidisciplinary data set that enables the regional extrapolation of shallow fault segments away from the mapped region described by Charzynski et al. (2019) and Cook et al. (2019). Shallow fault segments were interpreted using 3D seismic reflection data, as newly interpreted by Hennings et al. (2021), or as provided by operators, extracted unpublished records from the Railroad Commission (RRC) of Texas, as well as interpreted using linear patterns observed in interferometric synthetic aperture radar (InSAR) surface deformation measurements generated by Staniewicz et al. (2020). Many of these lineaments trend parallel to the map view patterns of the HypoDD-relocated TexNet hypocentral locations (Hennings et al., 2021).

Multiple earthquake catalogs, geomechanical parameters, and fault segments at shallow and basement levels were used as input for deterministic fault slip potential (DFSP) to establish their stability under present conditions and determine the change in pore pressure (ΔP_p) needed to push fault segments to criticality. Hennings et al. (2021) find that many segments at both levels of faulting have

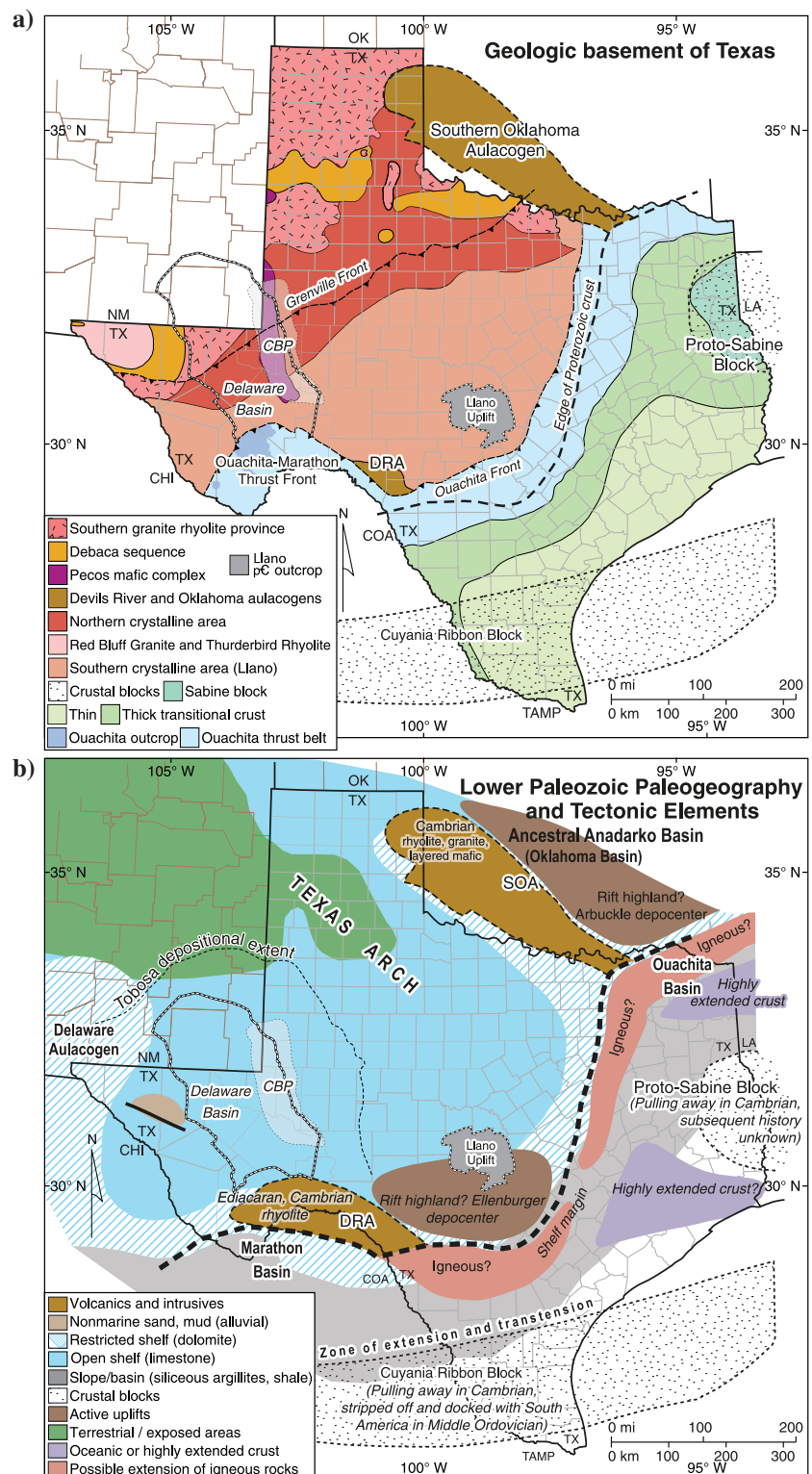


Figure 3. (a) Geologic basement map of Texas and (b) Cambrian and Paleozoic tectonic elements, paleogeography, and general configuration of the Tobosa Basin. Main tectonic elements are abbreviated. DRA, Devils River axis (or uplift); SOA, Southern Oklahoma Aulacogen. Shaded polygons represent the Ediacaran-Middle Cambrian depositional environments and rocks. Modified from Ewing (1991, 2019), Mosher (1998), Smye et al. (2019), and Horne et al. (2022).

DFSP values that would render the faults geomechanically stable under native conditions. However, as a population, the shallow faults require a far lower increase in ΔP_p to become unstable compared with most of the basement-rooted faults. Hennings et al. (2021) discuss how many of the earthquake sequences occur along the shallow faults, triggered by ΔP_p from shallow SWD and HF. Conversely, basement-rooted faults with unstable DFSP values are limited to well-oriented faults that are proximal to SWD into deep-injection intervals, most notably the Culberson-Mentone earthquake zone, a region experiencing an increased rate of seismicity and elevated magnitudes (M_L 4.6, 26 March 2020; M_L 4.4, 25 June 2021; M_L 4.3, 28 July 2021; M_L 4.3, 3 September 2021; M_L 4.1, 18 September 2021; M_L 4.3, 23 September 2021; M_L 4.2, 29 September 2021; M_L 4.0, 3 October 2021; M_L 4.0, 11 December 2021; and M_L 4.4, 16 December 2021) relative to other sequences in the seismogenic region of the Delaware Basin (Figure 1). The work presented by Hennings et al. (2021) provides datapoints, which support the hypothesis that the maximum earthquake moment magnitude is tied to the surface area and stiffness of country rock (Zoback and Gorelick, 2012); thus, favorably oriented basement-rooted faults have greater potential to host larger moments, as observed in the Culberson-Mentone earthquake zone; however, strata-bound shallow faults may only host lower moment magnitudes.

Although a regional map of shallow fault segments was constructed by Hennings et al. (2021), their interpretation was limited to a map view and did not include a thorough structural characterization of these segments. Therefore, the fault interpretations presented here represent a comprehensive update to the work outlined by Hennings et al. (2021). This research includes additional subsurface data, which was leveraged to update existing fault segments and identify previously unmapped fault segments. We integrated all available data and provided an interpretation of the 3D morphologic characteristics (e.g., strike, dip, length, vertical displacement, and surface area) of all shallow faults mapped across the basin to better understand seismogenic hazards within the Delaware Basin.

Database and methodology

This study focuses on the core of the seismogenic region of the Delaware Basin (Figure 1), which aerially extends across five counties in West Texas (approximately 18,500 km² [8500 mi²]). Shallow faults are interpreted using an integrated data set, and the aerial footprints of each data type are shown in Figure 4. These fault segments are locally controlled using 3D seismic reflection data volumes, either conducted by the authors or provided externally by petroleum operators. Regional patterns of faulting are observed through the integration of regional, linear surface deformation features observed from InSAR, earthquake hypocenters and slip-plane orientations calculated from focal mechanism solutions from multiple earthquake catalogs, and the digital integration of all publicly available data, including maps,

cross sections, existing fault interpretations, and interpretations from thousands of digital and raster well logs that were sourced from the Railroad Commission of Texas (2022) and IHS LogNet®.

Similar to other regionally integrated data sets, the ease of interpretation and confidence in the 3D character of shallow faults is reflective of the quality and distribution of control data (Figure 4). Regional data, including point locations of earthquake events (New Mexico Tech Seismological Observatory, 2021; TexNet, 2021), relocated earthquake catalogs (P. Li and A. Savvaidis, personal communication, 2021), and InSAR surface deformation estimates (Staniewicz et al., 2020), delineate the largest interpretation domain, which extends from the eastern margin of the Diablo platform to the western margin of the Central Basin platform and is herein referred to as the seismogenic region, as it extends over most of the earthquake sequences in the Delaware Basin (Figure 4; Table 1).

Shallow fault segments are classified according to levels in mapping confidence: high, moderate, and low. Fault segments interpreted with high confidence are supported by sufficient data to validate their mapped geometry (i.e., 3D seismic data, interpretations of which are completed in house, provided by operators, or published online). Fault segments interpreted with moderate confidence have varying degrees of uncertainty including their current mapped extent (length and height), geometry, lateral continuity, or specific placement, and are interpreted from patterns of InSAR surface deformation and/or alignment of well-located earthquakes. Low confidence fault interpretations lack sufficient evidence to warrant inclusion here.

In this study, the strength and quality of information obtained from each data source have been considered and delineated across the seismogenic region of the Delaware Basin. Inset regions informed by 2D (2Da–2Dd) and 3D (3Da–3Dc) data sets are shown in Figure 4. Data sources, interpretation methods, aerial coverage (individually and percentage of the total mapped region), as well as the number of faults mapped, and the resulting interpretation confidences for faults mapped within each data region are listed in Table 1.

Observations from 3D seismic data

Several 3D seismic reflection data sets were used to directly interpret and guide fault interpretations throughout the Delaware Basin. Fault segments within inset region 3Da were provided by petroleum operators and validated by the authors. Data regions 3Db and 3Dc are guided by depth-converted 3D seismic reflection data volumes and interpreted by the authors.

Interpretations from these three inset regions have the highest confidence and the finest scale of control. When combined, these 3D seismic regions extend more than 1889 km² (approximately 729 mi²), accounting for approximately 8% of the mapped region (Table 1; Figure 4). Interpretations gleaned from 3D seismic data provide context about morphologic heterogeneities and

deformation intensities that may be present throughout the basin.

In total, 211 fault segments were interpreted using local 3D high-resolution data sets and 210 faults outside of the seismic controlled regions. When summed, the regional fault interpretation accounts for 1085 km (approximately 675 mi) of fault length, compared with 663 km (approximately 412 mi) of fault length within the 3D seismic controlled regions (Table 2). Similar to other regional integrated mapping studies, the interpretation is limited to the data available; therefore, these lengths should be considered as minimum values, as there may be faults that are not detected using current data sources due to their limited resolution.

3Da Rojo-Caballos fields: Reeves and Pecos Counties, Texas

The first 3D seismic controlled inset area (3Da) covers 934 km² (approximately 361 mi²) of the southern Delaware Basin. This data region straddles the boundary between Reeves and Pecos Counties (Figure 4). Fault segments mapped within this data region are constrained by a proprietary depth-migrated 3D seismic reflection survey. There are 36 horizontal map-view fault segment traces that were interpreted using this 3D survey and the traces represent the intersection line between fault segment surfaces and the gridded top-DMG seismic horizon. These segments were interpreted by operators and converted into 3D objects by applying

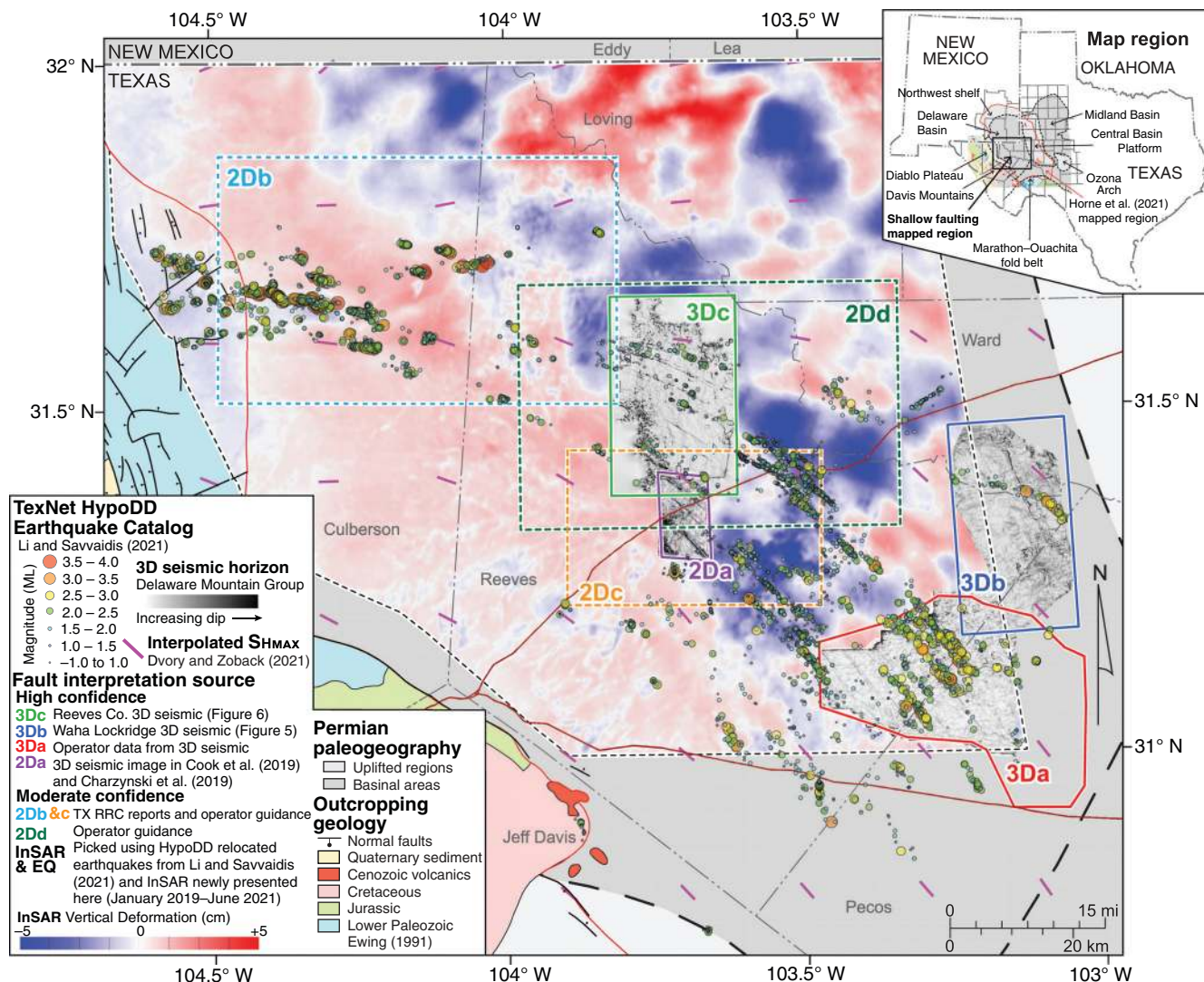


Figure 4. Index map of data set used to interpret shallow faults across the seismogenic region of the Delaware Basin. Regions of high and moderate mapping confidence data are outlined, and inset areas that are controlled by 3D and 2D data sources are labeled three dimensions and two dimensions, respectively. Examples of how gridded and dip-illuminated seismic horizons guide the interpretation of shallow faults are shown (modified from Charzynski et al., 2019; Hennings et al., 2021). A strong linear pattern of TexNet HypoDD relocated earthquake hypocenters (P. Li and A. Savvaidis, personal communication, 2021) in map view is shown, and these elongate narrow clusters of earthquakes run parallel to narrow, elongate features observed from an InSAR cumulative vertical deformation map (January 2019 and June 2021), newly presented here, following (Staniewicz et al., 2020).

Table 1. Data set and methodology used in the fault interpretation. The areal extent of each mapping region and number of faults split by high and moderate interpretation confidences are tabulated.

Mapping region, interpretation confidence, data set used, and methodology			Faults mapped		Interpretation region area		% of mapped region	Mapping confidence	
			#	% total	(km ²)	(mi ²)		#High	#Mod.
High	3Da Rojo-Caballos: data from 3D seismic interpretation provided by an operator and verified by the authors		36	9%	934	361	4.1%	36	—
	3Db Waha-Lockridge: interpretation of 3D seismic data completed by the authors		60	14%	469	181	2.1%	60	—
	3Dc Reeves County: interpretation of 3D seismic data completed by the authors		115	27%	486	188	2.1%	115	—
	2Da: interpretation gleaned from seismic image in Cook et al. (2019) and Charzynski et al. (2019)		14	3%	108	42	0.5%	14	—
Moderate	2Db: interpretation gleaned from georeferenced image from unpublished TX RRC report in Culberson County, Texas and operator guidance		31	7%	2527	976	11%	—	31
	2Dc: interpretation gleaned from georeferenced image from unpublished TX RRC report in Reeves County, Texas		17	4%	1002	387	4%	—	17
	2Dd: interpretation gleaned from georeferenced image provided by an operator		11	3%	2395	925	10%	—	11
Combined	InSAR surface deformation map and TexNet HypoDD relocated catalog		19	5%	22,850	8822	100%	19	—
	TexNet HypoDD Relocated Catalog		120	29%				—	120
Total (3D inset regions)			211	50%	1889	729	8%	211	—

Note: Inset region names, number of faults identified within each mapping region, fault mapping confidence, and colors referenced in later figures and tables also are indicated.

Table 2. Shallow fault mapping confidence, orientation, length, and interpretation datum summary.

Data region color and name	#	Mapping confidence		Fault orientation		Defined dip?	Fault segment length				Fault datum
		High	Mod.	Strike (°)	Dip (°)		Mean (m)	Max. (m)	Min. (m)	Sum (km)	
3Da	36	36	—	323	75	No	6510	15,739	1512	234	DMG
3Db	60	60	—	347	68	Yes	2296	10,536	360	138	DMG
3Dc	115	115	—	295	78	Yes	3250	2289	310	393	DMG and BSPG
2Da	14	14	—	300	75	No	5872	11,604	1618	82	DMG
2Db	31	—	31	58	80	No	5695	9726	3460	177	CASTILE and DMG
2Dc	17	—	17	301	75	No	6161	13,736	2659	105	DMG
2Dd	11	—	11	158	75	No	5468	11,047	2630	60	DMG
InSAR and HypoDD EQ	19	19	—	75	75	No	6348	10,600	3590	121	DEM
HypoDD EQ Catalog	120	—	120	323	75	No	4509	10,528	1622	451	DMG
Faults used in analysis	421	242	179	310	73	—	4152	19,498	427	2014	—

Note: Inset region names, number of faults identified within each mapping region, fault mapping confidence, and colors referenced in later figures and tables also are indicated.

Note: Inset region names, number of faults identified within each mapping region, fault mapping confidence, and colors referenced in later figures and tables also are indicated.

an average dip-angle normal to the trend of each trace. These fault segments were assigned a 72° dip across the data region, following the recommendations provided by the operator. A breakdown of the structural characteristics of faults mapped within the 3Da data region, including fault length and orientation (strike and dip), is outlined in Table 2. Other characteristics, such as fault surface area, and impacted strata (top DMG) are outlined in Table 3.

3Db Waha-Lockridge fields: Ward, Reeves, and Pecos Counties, Texas

The second detailed area uses an early 1990s vintage, 470 km² (approximately 181 mi²) 3D seismic reflection data volume (3Db) from Hardage et al. (1999) that covers the Waha-Lockridge oil fields in the southeastern Delaware Basin, straddling the boundaries separating Ward, Reeves, and Pecos Counties in West Texas (Figures 4 and 5a). The basement-rooted contractile deformation and depositional patterns have been described in the literature (Hardage and Major, 1998; Hardage et al., 1999; Haruna et al., 2014; Hardage, 2015; Horne et al., 2021). The process of interpreting shallow faults in this data set relied upon traditional seismic interpretation techniques, including the correlation of well tops to identify important faulted stratigraphic intervals, and interpreting horizons and faults on a variety of vertical seismic profiles to capture changes in fault trends. In addition, seismic attributes were extracted from the 3D auto-tracked and gridded top-DMG seismic reflector (Figure 5b and 5c). Using these techniques, 60 fault segments were mapped and characterized (Table 1). These faults are interpreted as parallel, north-northwest-striking, dip-slip faults. These faults are centered on the top DMG, where they have the greatest vertical offset, and generally, tip out vertically away from the DMG (Figure 5d and 5e). These faults are vertically decoupled from the basement-rooted fault segments mapped by Horne et al. (2021; Figure 5e). Structural characteristics including fault length, orientation, and datum are outlined in Table 2. Fault throw, impacted strata, and fault segment surface area are included in Table 3.

3Dc Central Grisham fault: Reeves County, Texas

The third area of detailed 3D seismic interpretation is referred to as 3Dc Reeves County. This data region contains a depth-migrated proprietary 3D seismic reflection volume that covers approximately 486 km² (approximately 188 mi²). This 3D survey straddles a central

portion of the Grisham fault zone (GFZ) within Reeves County (Figures 4 and 6a) and consists of a depth-migrated 3D seismic reflection volume that has undergone postvelocity seismic reprocessing by the operator. Similar to 3Db, this interpretation relied on the correlation of well tops to identify important faulted seismic

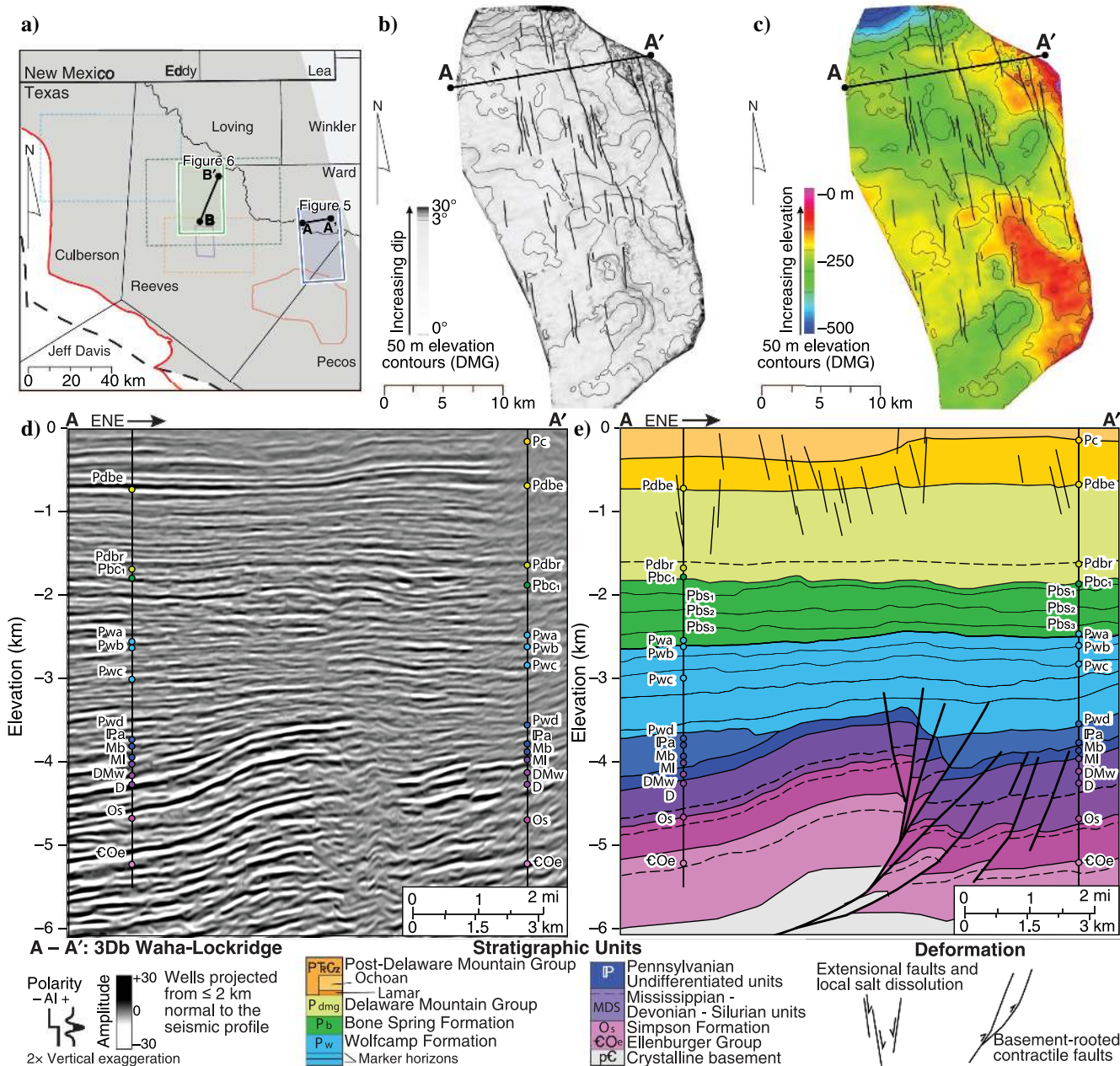


Figure 5. (a) Index map of data regions used to interpret shallow faults across the seismogenic region in the Delaware Basin. Sources of high and moderate mapping confidence data are outlined as solid and dashed rectangles, respectively. Areas that are controlled by 3D data that are interpreted by the authors and used for 3D faulted framework modeling are colored by respective data region (royal blue, 3Db Waha-Lockridge; green, 3Dc Reeves County). Examples of how the top DMG seismic horizon is used to map shallow faults in the 3Db Waha-Lockridge data region are shown as gridded surfaces highlighting variations in (b) dip and (c) elevation. Structural contours of the top DMG are shown in both images. (d) The uninterpreted seismic trace (A-A') is shown, formation tops are colored according to the stratigraphic unit, and wells that are located within 2 km of the profile are projected onto the section. Formation top interpretations are gleaned from Smye et al. (2021a) and Geological Data Services (GDS, now IHS Markit) (IHS Energy, 2009). Seismic trace (A-A') is fully interpreted in (e), which highlights the two structural styles observed in the basin: basement rooted and shallow faults.

stratigraphic intervals. Objects were mapped along inline, crossline, arbitrary, and fence profiles. Seismic attribute extractions performed on the 3D auto-tracked and gridded top DMG were especially helpful when mapping deformation (Figure 6b and 6c). As a result, 115 fault segments were interpreted within this data region (Table 1). Of these faults, 97 offset the DMG, seven of which extend through the DMG and into the underlying BSPG, which is only cut by 13 fault segment surfaces (Table 3). Fault segments interpreted from this seismic data set form a series of parallel, west-north-west-striking faults that are limited to the sedimentary section (Figure 6b, 6c, and 6e). Structural characteristics including fault length, orientation, and throw are outlined in Tables 2 and 3.

Integration of regional data

Cumulative vertical deformation between January 2019 and June 2021 over the central Delaware Basin highlights elongate and narrow linear deformation features that align parallel to earthquakes detected by TexNet (Figure 4). The up- and downthrown sides of fault segments interpreted from the InSAR surface deformation map are observable in the map view (Figures 4 and 7).

Earthquake hypocentral locations also were used as input for shallow fault mapping. Specifically, dense, linear sequences of earthquake hypocenters that cluster in elongate linear patterns with similar elevations define the traces of 140 fault segments, 19 of which also are mapped by patterns illuminated from InSAR surface deformation observations. Although there is large uncertainty in the depth of the earthquakes (mean depth

uncertainty of 3.6 km), a recent publication by Li and Savvaidis (2021) provided a HypoDD relocated earthquake catalog; thus, XY and Z locations are more meaningful. Patterns observed from the InSAR surface deformation map and HypoDD relocated earthquakes are consistent with orientations mapped using 3D seismic reflection data sets, corroborating this interpretation. Furthermore, many of the fault segments mapped from InSAR were mapped and published by Hennings et al. (2021); however, these traces were subsequently modified, and 3D characteristics were applied to each mapped segment deterministically in this study.

Segments mapped using either InSAR or earthquake locations lack sufficient dip constraints. For this reason, fault traces mapped exclusively from HypoDD earthquake hypocentral locations are deemed as moderately confident fault interpretations, and faults that are mapped using HypoDD earthquake hypocentral locations and InSAR surface deformation measurements are considered as high-confidence interpretations (Table 1; Figure 7).

Specifically, dip angles for fault segments mapped using InSAR surface deformation measurements, 2D published and unpublished images, and earthquake hypocentral pointsets are difficult to determine due to insufficient data. Fault planes were generated from 2D polyline interpretations for each of these data regions using a technique that applies an average dip angle normal to the trend of each line (Table 2).

Table 3 breaks down the stratigraphic interval of faulting and datum of fault interpretation. Fault segments interpreted from a combination of InSAR observations and

Table 3. Shallow fault orientation, length, surface area, throw, and summary of impacted stratigraphic intervals.

Data region color and name	#	Mapping confidence		Fault segment length				Fault surface area (km ²)				Throw (m)			Stratigraphic interval of faulting				
		high	mod.	Mean (m)	Max. (m)	Min. (m)	Sum (km)	Mean	Max.	Min.	Sum	Mean	Max.	Min.	Supra-DMG	DMG	Intra-DMG	BSPG	DMG and BSPG
3Da	36	36	—	6510	15,739	1512	234	11	27	2.6	395	N/A	N/A	N/A	—	36	—	—	—
3Db	60	60	—	2296	10,536	360	138	2	11	0.3	133	17	64	3	—	60	—	—	—
3Dc	115	115	—	3250	2289	310	393	3	24	0.2	300	29	89	7	—	106	2	13	7
2Da	14	14	—	5872	11,604	1618	82	7	14	1.9	99	N/A	N/A	N/A	—	14	—	—	—
2Db	31	—	31	5695	9726	3460	177	11	19	6.9	353	N/A	N/A	N/A	13	18	—	—	—
2Dc	17	—	17	6161	13,736	2659	105	8	30	3.2	140	N/A	N/A	N/A	—	17	—	—	—
2Dd	11	—	11	5468	11,047	2630	60	11	22	4.1	116	N/A	N/A	N/A	—	11	—	—	—
InSAR and HypoDD EQ	19	19	—	6348	10,600	3590	121	12	21	7.1	1079	N/A	N/A	N/A	19	—	—	—	—
HypoDD EQ Catalog	120	—	120	4509	10,528	1622	451	9	21	3.2	235	N/A	N/A	N/A	—	120	—	—	—
Faults used in analysis	421	242	179	4152	19,498	427	2014	7	30	0.2	2849	25	89	3	Supra-DMG: 32	DMG: 382	BSPG: 7		

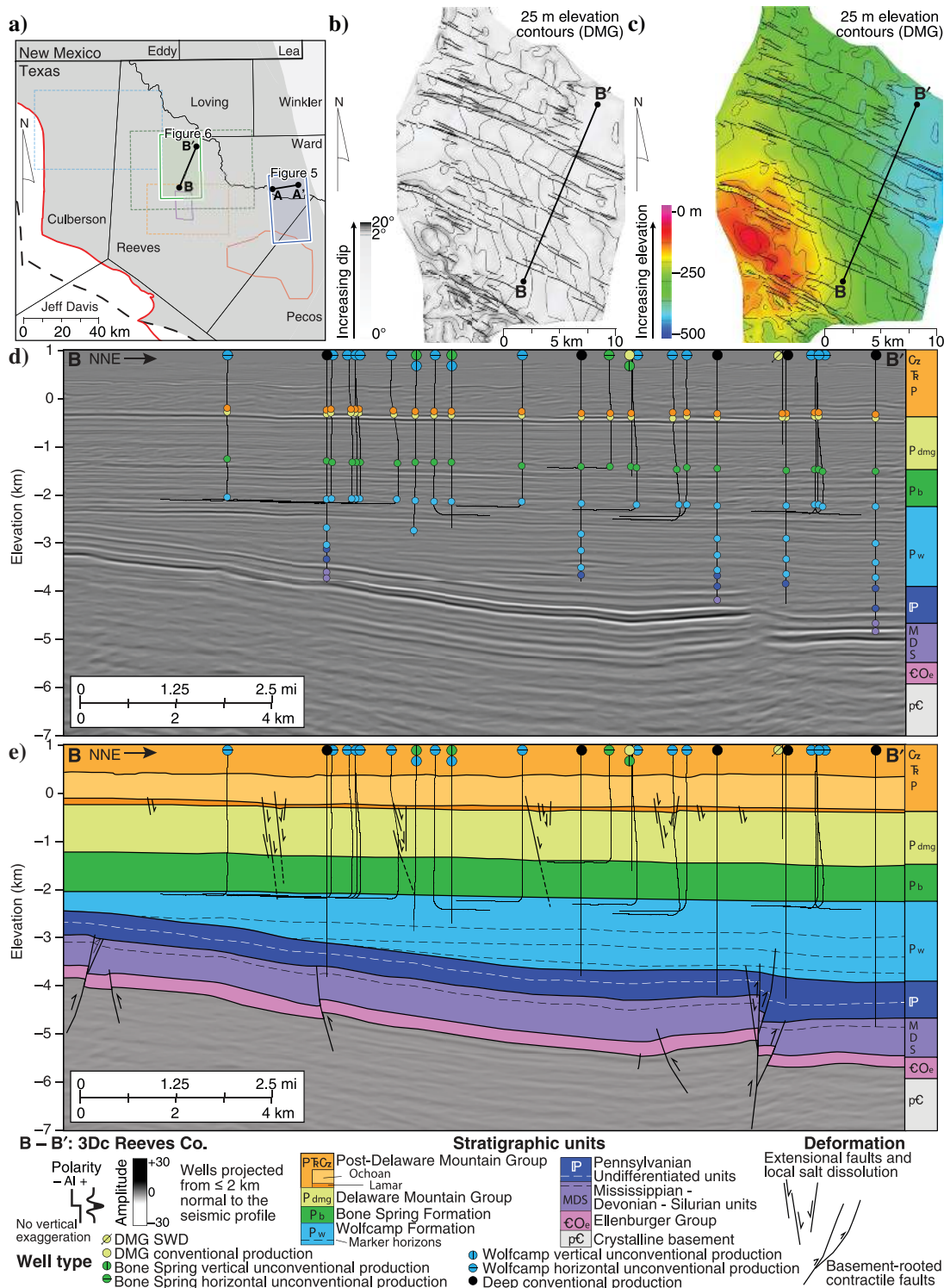


Figure 6. (a) Index map of data regions used to interpret shallow faults across the core seismogenic region in the Delaware Basin. Sources of high and moderate mapping confidence data are outlined as solid and dashed rectangles, respectively. Areas that are controlled by 3D data that are interpreted by the authors and used for 3D faulted framework modeling are colored by respective data regions (royal blue, 3Db Waha-Lockridge; green, 3Dc Reeves County). Examples of how the top-DMG seismic horizon is used to map shallow faults in the 3Dc Reeves County data region are shown as gridded surfaces highlighting variations in (b) dip and (c) elevation. Structural contours of the top DMG are shown in both images. (d) The uninterpreted seismic trace (B-B') is shown, formation tops are colored according to the stratigraphic unit, and wells that are located within 2 km of the profile are projected onto the section. Formation tops are extracted from Smyre et al. (2021a), GDS (now IHS Markit) (IHS Energy, 2009). Seismic trace (B-B') is fully interpreted in (e), which highlights the two structural styles observed in the basin: basement rooted and shallow faults. Wells that are projected onto the section are labeled according to type (SWD, conventional, and unconventional) and target interval (modified from Hennings et al., 2021).

HypoDD relocated earthquake catalog use ground elevation from a digital elevation model (DEM) as a datum. These traces are projected downward from the DEM at an average dip angle, perpendicular to the strike orientation of 2 km into the subsurface. As these are interpreted as elongate graben features, an average dip derived from high-confidence interpretations from 3Db to 3Dc is applied (75°). Key seismic stratigraphic horizons, fault surface extents, fault-horizon offset, and key tectonostratigraphic patterns provide evidence for fault growth and linkage evolution.

Summary of subsurface interpretation domains

A new map of shallow faults that extends across the core of the Delaware Basin has been generated and comprehensively characterized. In total, 36 2D fault traces were provided by industry operators within 3Da Rojo-Caballos and 175 faults were mapped and characterized

from the 3Db Waha-Lockridge and 3Dc Reeves County seismic surveys. Observations from these three data regions were relied upon to provide expected morphologic variations of the degree of faulting and fracturing of the DMG across the seismogenic region. These data sets underscore the subtle, but important, deformation patterns that align with modern surface motion detection and well-located earthquake hypocenters, corroborating the use of both data sets to map deformation.

Fault segment surfaces interpreted from 3D seismic data are considered high-confidence interpretations, and fault segments gleaned from published maps from literature (e.g., Charzynski et al., 2019; Cook et al., 2019; Hennings et al., 2021), unpublished permitting report filings submitted to the Railroad Commission of Texas (2022), and provided to the authors from operators have been modified, superseded, or used as is and are considered as moderate confidence interpretations.

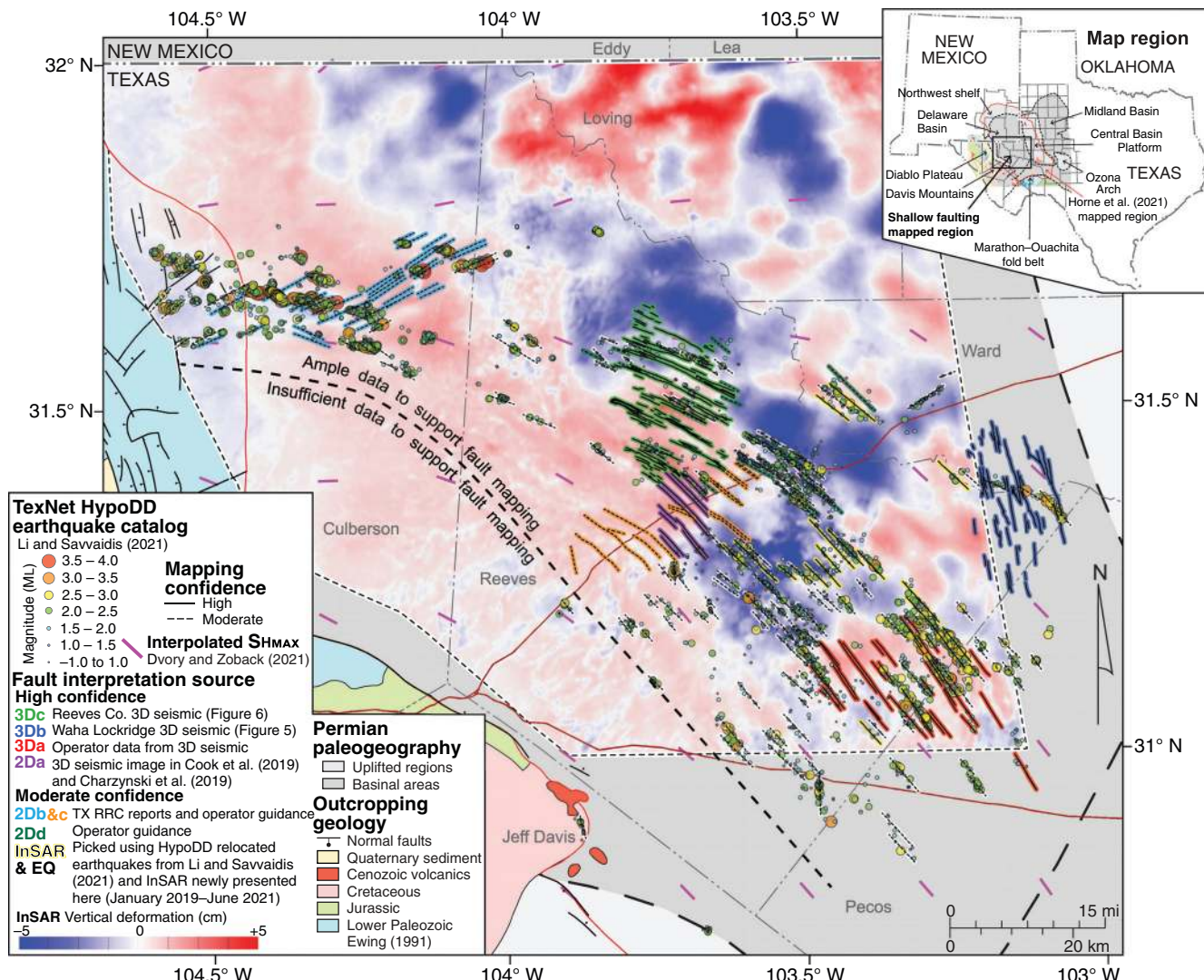


Figure 7. Fault interpretation of the core seismogenic region of the Delaware Basin. Fault traces are colored by data sources. TexNet HypoDD relocated earthquakes are shown (P. Li and A. Savvaidis, personal communication, 2021) and a newly generated InSAR cumulative vertical deformation map (January 2019–June 2021) highlights the strong alignment with HypoDD relocated earthquake hypocentral locations.

Fault segments mapped using InSAR and TexNet 3D hypocentral data are considered high-confidence interpretations, whereas segments interpreted using the two data sets independently are considered moderate confidence interpretations (Table 1; Figure 7). This fault map has 421 fault segments, 242 are considered high confidence, and the remaining 179 are moderate confidence (Figure 7).

In this study, we convert map view fault traces into 3D fault segment surfaces following the methods outlined by Horne et al. (2020, 2021). Faults traces compiled from published data sets (Charzynski et al., 2019; Cook et al., 2019; Hennings et al., 2021), TX RRC reports, and dense linear clusters of HypoDD relocated earthquakes use the top DMG regional surface as a datum (Table 2). This regional surface was gridded from 980 well top penetrations extracted from Smye et al. (2021a). Fault segment traces that are interpreted from InSAR ground deformation anomalies (Staniewicz et al., 2020) use a regional DEM as a datum.

Fault segments mapped using 3D seismic reflection surveys are shown in the map view (Figure 7), and these segments represent the intersection line between the fault surface and the downthrown hanging wall of the faulted top-DMG stratigraphic horizon. The 3D morphologic characteristics including orientation (strike and dip), downdip height, vertical displacement (throw), horizontal length, and surface area are observed in-house interpreted 3D seismic regions (3Db and 3Dc). To generate fault segments surfaces that are representative of the segment surfaces interpreted using 3D data, an average downdip height of 2000 m was assigned to fault segments lacking 3D control. Specifically, fault segments mapped using the DMG as a datum (3Da, 2Da–2Dad, and TexNet HypoDD relocated catalog) were projected at an angle normal to their trend greater than 500 m, and below 1500 m from the DMG horizon-fault interface. Fault segment traces interpreted from the InSAR surface deformation map are projected at an angle normal to their trend from ground surface elevation down 2000 m into the subsurface. The datum used for each interpretation is listed in Table 2 and the details for the stratigraphic interval of faulting are provided in Table 3.

Although there is sufficient evidence for the presence of shallow faulting across the mapped region, the generation of 3D water-tight faulted framework models as defined by Krantz and Neely (2016) was limited to 3D seismic interpreted data regions (3Db and 3Dc); therefore, fault attribute interrelationships using fault throw are not calculated for segments outside of these data regions. A summary of fault segment, lengths, surface areas, and offset measurements within the 3D seismic controlled inset area is shown in Table 3. The spatial distributions of fault segments and 3D fault-segment surfaces are shown in Figures 7 and 8, respectively. Fault segment surfaces interpreted directly from 3D seismic data, as well as converted from 2D objects to 3D planes using the methods as previously described, have

been modeled to have gridded cells with 100 m equant triangles, enabling a consistent static structural characterization of fault strike, dip, trace length, and surface area. Figure 7 also shows that there is a boundary southwest and west of the interpretation regions where we do not have sufficient data control to map faults; however, we interpret this region to be faulted.

Structural characterization

Fault characteristics

A 3D structural model of shallow faults in the Delaware Basin was generated that has 421 fault segment traces that trend north-northwest–south-southeast in the southeast (e.g., northwestern Pecos County, southern Ward County, and southeastern Reeves County), rotating to west-northwest–east-southeast in Reeves County, and west-southwest–east-southeast in Culberson County (Figure 7). Fault orientations, and lateral and vertical extents, are deterministic in regions benefiting from 3D seismic data (3Db Waha-Lockridge and 3Dc Reeves County) and conservatively modeled elsewhere.

Many of these fault segment surfaces form conjugate fault pairs that produce a series of elongate low-relief graben (Figure 7). Of the 421 fault segments mapped, 389 (92%) are interpreted to offset the DMG (Table 3). Deformation along these faults is subtle and best viewed using 3D seismic reflection data sets. Although vertical offset measurements are limited to the seismic horizon that corresponds with the top DMG, where data resolution allows, these faults have been observed to extend up into overlying units, and down into the BSPG (Figure 6d and 6e).

Strike and dip

Variations in fault geometry can be observed in which 3D seismic data are used in the interpretation, i.e., in the 3Db Waha-Lockridge and 3Dc Reeves County faults. The Waha-Lockridge fault set is oriented north-northwest–south-southeast with an average strike of 347° (Figure 8a). Faults dominantly dip toward the east (Figure 8b) and range in dip from 55° to 85°, with a mean of 68° (Figure 8c; Table 2). Conversely, faults interpreted from 3Dc Reeves County strike west-northwest–east-southeast, with an average strike of 295° (Figure 9a). These faults form conjugate sets, southeast-striking faults dipping toward the northwest-striking faults (Figure 9b). Faults mapped within this data set have slightly steeper dips, with a range of 65°–90°, with a mean of 78° (Figure 9c; Table 2). Together, fault segment surfaces interpreted from 3Db to 3Dc have an average dip of approximately 75°, which is used as input to fault segment interpretations lacking sufficient 3D control (Table 2).

Shallow fault segment geometries for the regional population are shown in map view Figure 10a. Fault segments strike northwest–southeast, with a larger percentage of faults striking northwest (Figure 10b). These fault segment surfaces have a narrow range in dip magnitude (Table 2), with an average dip of approximately 73° (Figure 10c). The number of segments within a fault

family and their structural attributes, such as orientation (strike and dip), length, surface area, throw, mapping confidence, and impacted stratigraphic units, has been tabulated in Tables 2 and 3.

Trace-length analysis

Fault segments within the subsurface faulted framework model range in length from approximately 0.3 to more than 15 km (approximately 0.2–9 mi). The mean

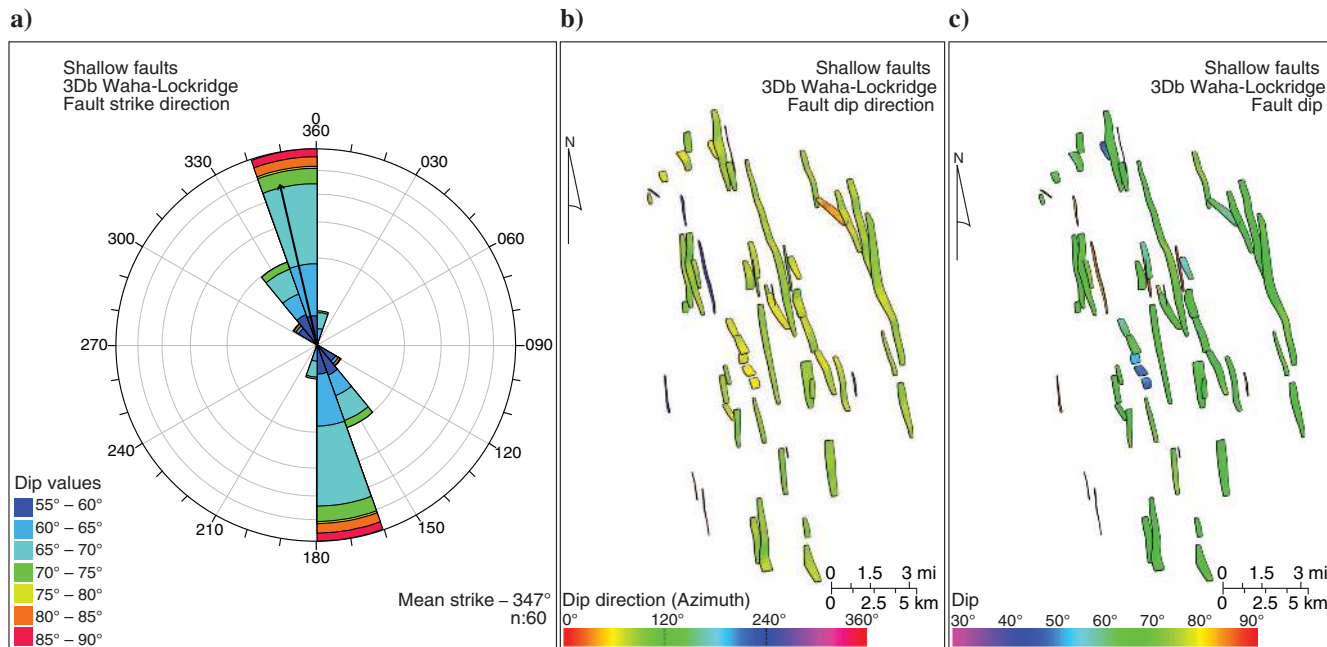


Figure 8. (a) Rose diagram showing a range of fault-strike directions for faults mapped in the Waha-Lockridge 3D seismic survey (3Db). Petals are colored by a range in dip magnitude (55°–90°). The black arrow points in the direction of the mean strike. (b) Aerial view of fault segment surfaces mapped in the 3Db Waha-Lockridge data region, colored dip direction, and (c) dip angle. Aerial images provide insight into subtle morphological variations in the shallow faults mapped in the Delaware Basin.

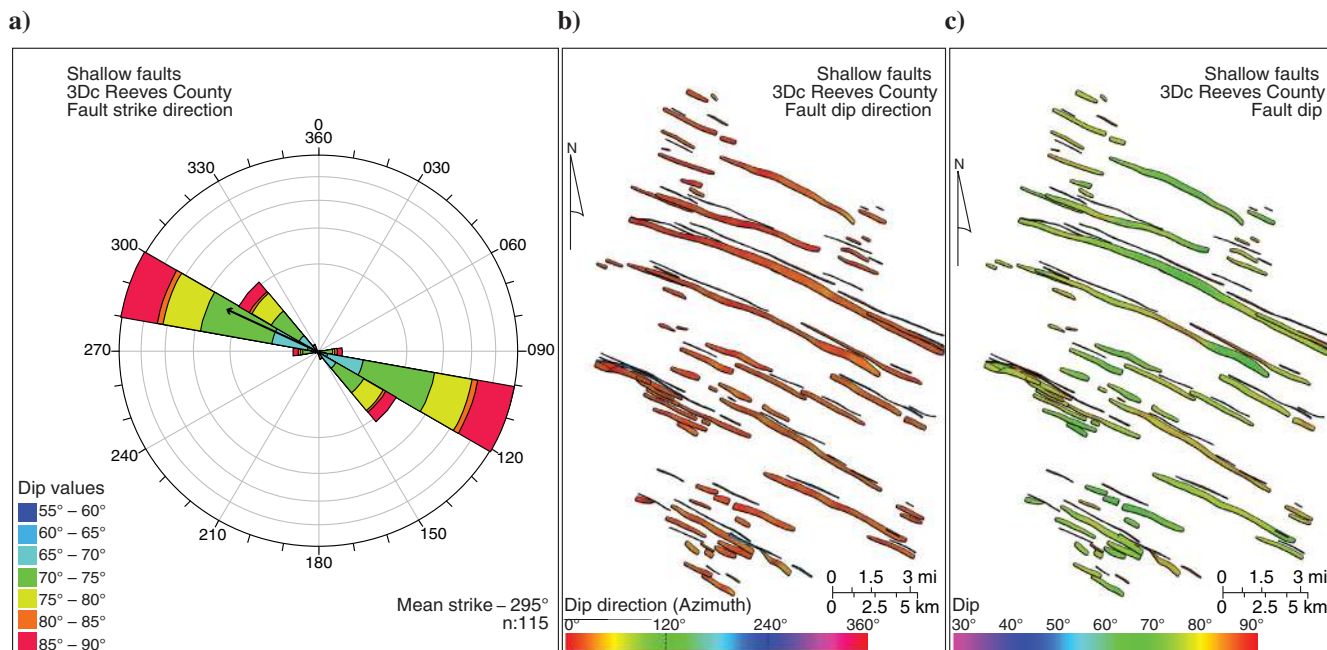
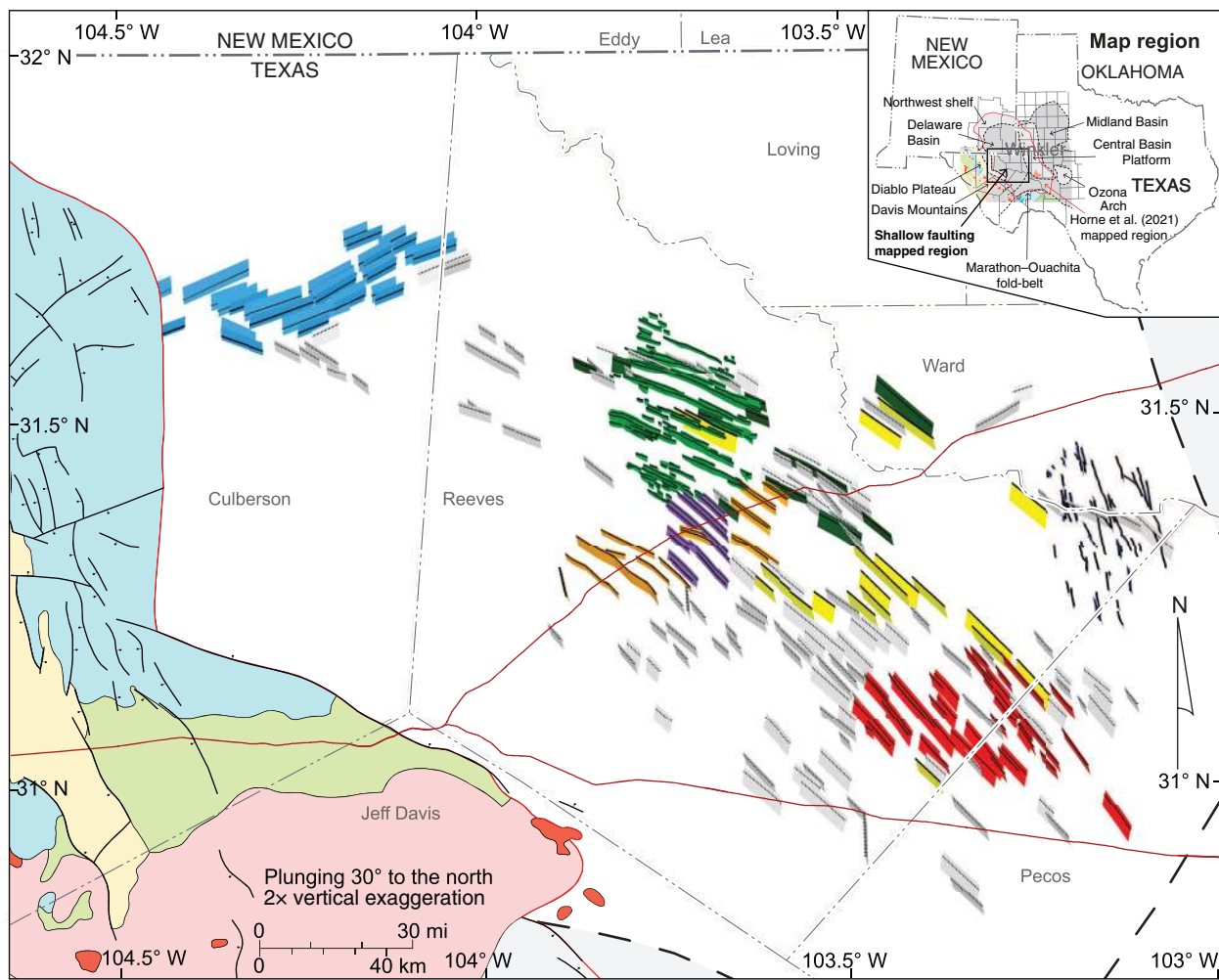


Figure 9. (a) Rose diagram showing a range of fault-strike directions for faults mapped in the Reeves County 3D seismic survey (3Dc). Petals are colored by a range in dip magnitude (55°–90°). The black arrow points in the direction of the mean strike. (b) Aerial view of the 3Dc Reeves County fault set, colored dip direction, and (c) dip angle. Aerial images provide insight into subtle morphological variations in the shallow faults mapped in the Delaware Basin.

a)

**Permian paleogeography**

- Uplifted regions
- Basinal areas

Outcropping geology

- Normal faults
- Quaternary sediment
- Cenozoic volcanics
- Cretaceous
- Jurassic
- Lower Paleozoic
- Ewing (1991)

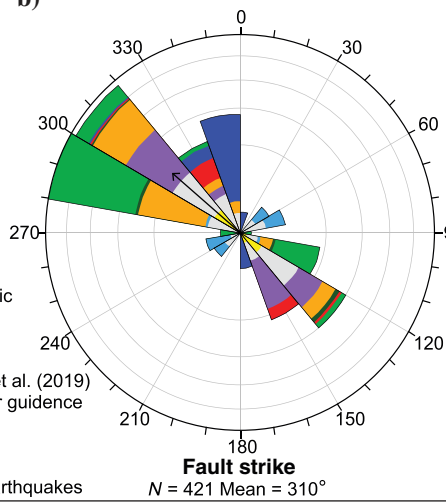
Mapping confidence

- High --- Moderate

Shallow fault surfaces**Interpretation sources**

- 3Da – Operator data from 3D seismic
- 3Db – Waha-Lockridge 3D seismic
- 3Dc – Reeves County 3D seismic
- 2Da – 3D seismic image from Cook et al. (2019) and Charzynski et al. (2019)
- 2Db – TX RRC reports and operator guidance
- 2Dc – TX RRC reports
- 2Dd – Operator guidance
- EQ – HypoDD earthquakes
- InSAR & EQ – InSAR & HypoDD earthquakes

b)



c)

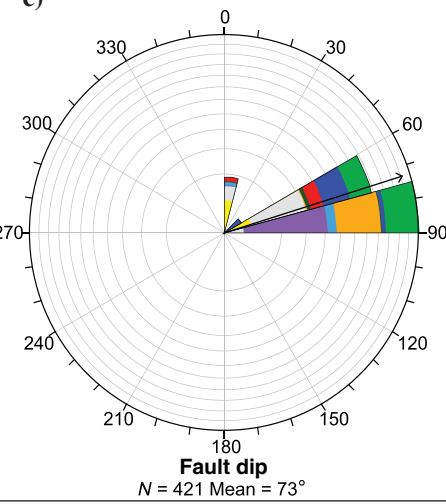


Figure 10. (a) Oblique regional view of fault segment surfaces interpreted throughout the core seismogenic region of the Delaware Basin. Fault surfaces are colored by data sources, and black solid and dashed traces represent high and moderate confidence interpretations, respectively. Fault segment surfaces mapped in interpretation region 3Db Waha-Lockridge have short surface heights and are oriented north-northwest–south-southeast, thus appearing as lines rather than surfaces. (b) Unidirectional rose diagram displaying the distribution of fault-strike orientation. Petals are colored by interpretation group and the black arrow points in the direction of the mean strike. (c) Unidirectional rose diagram showing a range of dip angles for faults mapped. Dip magnitudes range of 55°–90°. Petals are colored by interpretation group and the black arrow points in the direction of the average dip.

and range of length values for faults mapped within each data region have been tabulated in Table 2. Fault segments are classified as high and moderate confidence interpretations reflecting differences in control data density. The minimum length of a fault map is dependent on the resolution of the data (e.g., Table 1; Figure 5). Furthermore, 89% of faults mapped and qualified as high-confidence interpretations are interpreted from high-resolution 3D seismic reflection data sets. The remainder of high-confidence faults and all moderate confidence fault segments is reliant on the combined resolution of their respective data source (e.g., published fault maps, fault maps submitted in unpublished reports, earthquake hypocentral locations, and InSAR observed linear deformation features). Figure 11 shows the cumulative frequency of fault trace-length distribution for all shallow faults in the mapped region, as well as the distribution of fault length present between high and moderate confidence fault populations. Due to the varying and uneven resolution of the data supporting moderate confidence fault segments, the minimum segment length detected is generally ≥ 1.5 km (approximately 1 mi). Conversely, high-resolution 3D seismic data sets provide more control, enabling fault segments as short as ≥ 0.3 km (approximately 0.2 mi) to be

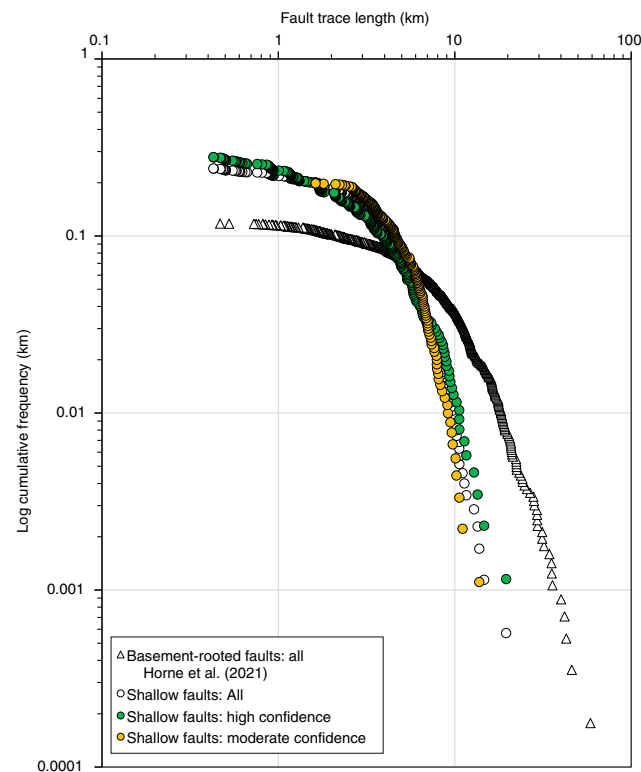


Figure 11. Cumulative fault trace-length frequency plot. There are three populations of newly presented shallow faults shown as circles; these include green, high-confidence interpretations; amber, moderate confidence interpretations; and white, all shallow faults mapped. This shallow fault length frequency distribution overlies the fault length frequency distribution of all basement-rooted faults mapped by Horne et al. (2021), which are shown as white triangles.

mapped (Figure 11). In addition to having the shortest segment length, the longest fault segment mapped also is considered a high-confidence interpretation. This longest fault is 19 km (approximately 12 mi) in length and was interpreted with the 3Da Rojo-Caballos data region. The 3D seismic reflection data sets interpreted by the authors (e.g., 3Db Waha-Lockridge and 3Dc Reeves County) show the widest variation in fault lengths, whereas fault interpretations provided by operators in the data region 3Da Rojo-Caballos most closely align with the maximum, mean, and minimum length distribution of faults incorporated from published and newly mapped interpretations leveraging one or more regional data sources (Table 2). The cumulative frequency of fault trace lengths for the full shallow fault population, as well as for faults that offset the DMG and BSPG for data regions 3Db Waha-Lockridge and 3Dc Reeves County is shown in Figure 12. Figure 12 shows the overlap in horizontal length between the regional population and shows that faults that offset the BSPG are the shortest fault population. Notably, shallow fault segments that offset the DMG within 3Db Waha-Lockridge and 3Dc Reeves County have similar length distribution to the full fault population.

Local faulted framework modeling

Two 3D faulted framework models have been constructed using interpretations from 3D seismic reflection data sets. These faulted framework models focus on the upper-Permian age stratigraphic intervals, mainly the DMG and top BSPG. The 3D gridded surfaces of the DMG have been interpreted as part of the fault framework interpretation process using 2D and 3D data sets and well top correlations (e.g., Figures 5 and 6). To better understand the nature of shallow, extensional deformation across the seismogenic region of the Delaware Basin, a regional, surface of the top DMG was gridded (Figure 12) using formation tops that have been interpreted from well-log data and published (Smee et al., 2021a). In general, the top DMG gradually deepens toward the western margin of the Central Basin platform.

Throw distribution

To characterize the distribution of displacement, we determined fault throw versus length (T-L) for each fault family offsetting the DMG, as well as the BSPG. For comparison, the regional distribution of fault throw interpreted to offset the top-Ellenburger Group (ELBG) along basement-rooted fault surfaces across the Delaware Basin and Central Basin Platform also is shown (Figure 13; Horne et al., 2021).

Although faults are mapped across the core area of the Delaware Basin, the assessment of throw is only conducted over the inset regions controlled by 3D seismic reflection data, including 3Dc Reeves County and 3Db Waha-Lockridge. Shallow faults that cut the DMG have the greatest throws; however, our sample size is limited. In some instances of linked-fault segments, maximum throw occurs at the fault-segment linkage zone. Maxima, minima, and mean fault throw values for each fault

family are summarized in Table 3. The confidence in each fault throw measurement is directly tied to the level of confidence assigned to the fault segment reflecting its respective source. Maximum throw (T) has been plotted against segment length (L) to better understand growth histories (Figure 13).

Diagrams showing fault array geometry and the distribution of extension depict the changes in the spatial character of the faults within data regions 3Db Waha-Lockridge and 3Dc Reeves County (Figures 14 and 15). These fault offset-based syntheses use a grid of parallel-trending equally spaced cross-section traces, which trend orthogonal to the mean strike of shallow faults within each data region. The offset sampling traces are spaced every 1 km and record the hanging-wall and footwall horizon-fault elevations as well as the apparent throw for the sampled shallow faults.

Shallow faults within 3Db Waha-Lockridge are sampled from south-southeast to north-northwest on a

series of sections that trend 81° (Figure 14a). Fault segments mapped in the north-northeastern portion of the interpretation region have the greatest vertical displacement and do not overly major basement-rooted faults (Figure 14b). The fault-related extension is the summation of the apparent extensional heave accommodated on the faults sampled by the 1 km spaced, 81° aligned cross sections. This extensional strain is greatest at the 19 km sample grid line, where the summed apparent throw for shallow faults is >270 m (Figure 14c and 14d). Notably, the fault array summation plots shown in Figure 14b and 14c are anticorrelated to the distribution of apparent throw along basement-rooted faults (Horne et al., 2021) and shallow faults, further documenting the decoupled relationship between the two fault systems.

Shallow faults within 3Dc Reeves County are sampled every 1 km from southeast to northwest on a series of sections that trend 24° (Figure 15a). Shallow faults with the greatest vertical displacements occur on elongate,

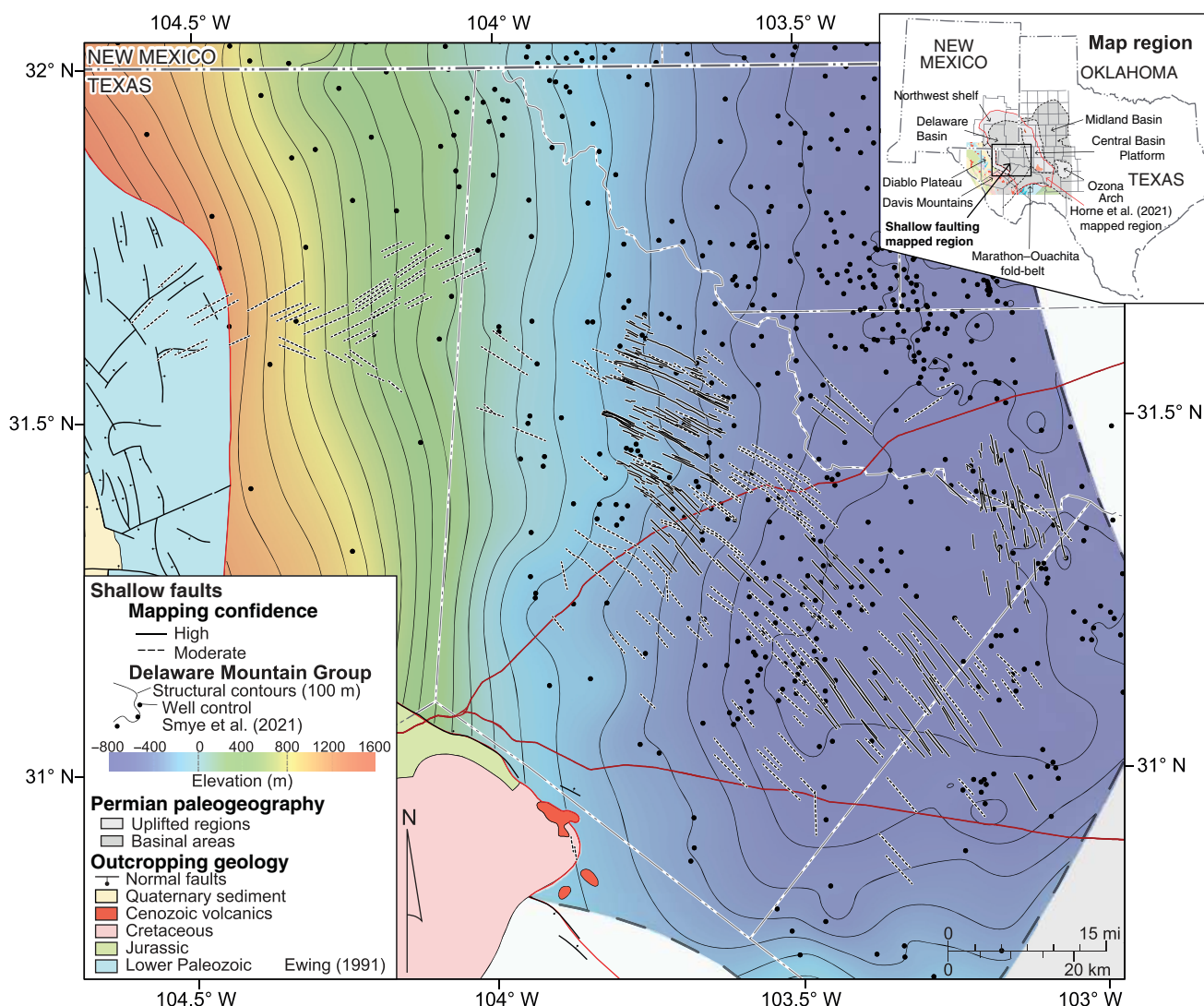


Figure 12. Structural map of top DMG in the central Delaware Basin. Shallow faults are shown and formation tops that guide this interpretation are extracted from Smyre et al. (2021a).

east-southeast-striking faults that dip toward the southwest (Figure 15b). Moreover, we observe waxing and waning throw gradient changes along the strike of the mapped fault surface, which may indicate that the surface is composed of short parallel-trending hard- and soft-linked faults. The lateral summation of apparent fault throw and extension is shown in Figure 15c and 15d. We observe a broad plateau of extensional strain, which extends across much of the fault array summation grid (Figure 15c and 15d). The apparent throw of each fault segment is summed to generate a cumulative apparent throw value to observe changes in throw across the data set; here, we observe a rapid decrease in an apparent throw at the northwestern and southeastern margin of the data set, which may be due to data truncation. In contrast to the fault array summation plots completed for data region 3Db Waha-Lockridge, we do not observe an inverse correlation between the magnitude of basement-rooted deformation and shallow faulting (Figure 15b and 15d).

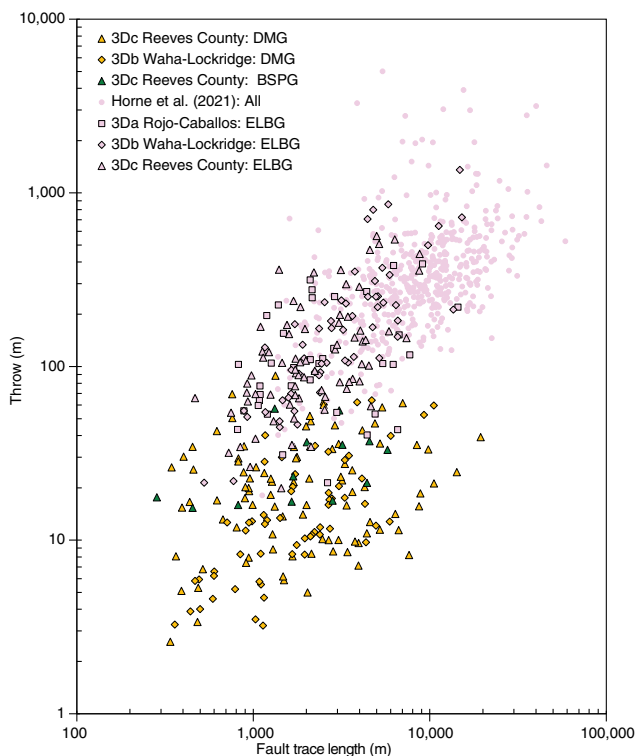


Figure 13. Fault trace length versus maximum throw for faults mapped at all levels across the Delaware Basin and Central Basin platform. Newly presented shallow faults overlay fault basement-rooted faults mapped by Horne et al. (2021). Fault symbol shapes represent data regions: squares, 3Da Rojo-Caballos; diamonds, 3Db Waha-Lockridge; triangles, 3Dc Reeves County; and circles, all basement-rooted faults mapped and modeled by Horne et al. (2021). Symbols are colored by the datum of interpretation: amber, DMG; dark green, BSPG; and pink, ELBG. Legend abbreviations include BSPG, Bone Spring Formation; DMG, Delaware Mountain group; and ELBG, Ellenburger group.

Discussion

Initiation and growth of shallow faults

There are 421 shallow fault segment traces, with mapped trends that rotate progressively from north-northwest–south-southeast in the southeast, to west-northwest–east-southeast in the northwest, and west-southwest–east-southeast to the north of the GFZ, in the region referred to as the Culberson-Mentone earthquake zone (Figure 16). The development of these shallow faults is primarily attributed to regional extension and exhumation from basin and range extension and the Rio Grande rifting (Henry and Price, 1986; Brown, 2019; Ruppel, 2019b), but may have initiated as fracture zones that formed and reactivated in response to late Permian and Triassic uplift, Mesozoic rifting events along the Gulf Coast margin, flexural extension and compressional reactivation of Paleozoic faults from Eocene-Oligocene age Laramide orogeny (e.g., Figure 3).

These shallow faults are interpreted as elongate, high angle, low dip-slip vertically offsetting features that are observed to be limited to the uppermost Permian-age strata, including the Guadalupian-age DMG, with some segments extending upward into the Ochoan-age units, and downward into the Leonardian-age BSPG. Specifically, these subtle elongate extensional features are clearly observed by generating 3D gridded surfaces from strong seismic reflectors in the DMG and BSPG; however, this seismic signal is reduced with depth (e.g., Figures 5 and 6). Charzynski et al. (2019) hypothesize that some of these segments, or vertically offset similar trending segments, may impact the Wolfcamp interval; however, the offset of these faults may be too small to resolve at the top of the Wolfcamp Formation. Cook et al. (2019) apply seismic attribute analyses and well production data to identify the vertical extent of these shallow faults. Specifically, horizontal transverse isotropic velocity variation with azimuth and amplitude variation with azimuth prestack attributes on a 3D seismic reflection data set in Reeves County (herein referred to as data region 2Da) illuminated a series of vertically stacked open fracture networks, which extend from the DMG, BSPG, and as deep as the Wolfcamp Formation. We use this work by Charzynski et al. (2019) and Cook et al. (2019) as an analog and presume that the vertically stacked nature of the open fractures mapped is not unique to data region 2Da. The 3D seismic reflection data show that these faults are present throughout the basin and there is a notable variation in their trend, with segments rotating with and parallel to changes in the direction of the principal horizontal stress $S_{H\max}$. Likewise, the presence and variation in the trend of these fault systems are observed in the InSAR surface deformation map and in HypoDD-relocated TexNet hypocentral locations (e.g., Figure 16).

In addition to faults tracking subparallel to $S_{H\max}$, there is no resolved amount of shear stress observed in 3D seismic data (e.g., 3Db Waha-Lockridge and 3Dc Reeves County), supporting the interpretation that these unique faults are extensional in origin. Charzynski

et al. (2019) and Cook et al. (2019) hypothesize that these graben features initiated as extensional vertical fracture systems, which conducted the formation of water and H₂S from deeper intervals. They speculate that, through time, these vertical fracture zones evolved into karst corridors, as these fluids have compromised the integrity of carbonate and evaporite strata along the flanks of the vertical fractures through dissolution.

Analysis of fault attributes including horizontal trace length (L) and vertical displacement (throw, T) is commonly used to describe the growth evolution of a fault system, where fault displacement is consistently a small fraction of fault length (Cowie and Scholz, 1992; Schultz et al., 2008; Gudmundsson et al., 2013). The horizontal trace length (L) of all faults was plotted (Figure 11) and the horizontal trace length (L) and vertical displacement (throw, T) for faults mapped using 3D seismic reflection data sets (3Db Waha-Lockridge and 3Dc Reeves County) were investigated to characterize the distribution of displacement within each inset region (Figure 13). The T-L plot in Figure 13 shows that fault segments mapped in 3Db Waha-Lockridge and 3Dc Reeves County have disproportionately small throws given their length.

In addition to being underdisplaced, these faults are overly steep (mean segment dip approximately 75° from horizontal) compared with ideal normal faulting conditions (Anderson, 1951). The shallow faults appear to be neotectonically active, with many segments spatially correlated with elongate patterns in HypoDD relocated earthquake catalog (P. Li and A. Savvaidis, personal communication, 2021) and InSAR deformation observations (Staniewicz et al., 2020). Although these characteristics seem anomalous, they may be the product of mechanical stratigraphic control on fault growth related to the faults cutting the relatively brittle DMG with more ductile under- and overlying units mechanically restricting discrete propagation of slip surfaces and horizon offset into those units (e.g., Ferrill et al., 2017).

The under displacement of these faults may be the result of multiple parallel-trending segments that are linked, forming longer faults. These many-segmented fault zones also may include significant antithetic faults that reduce the overall displacement and may explain the narrow-graben features captured using InSAR data (e.g., Figure 16). This oversteepening of fault segments may be explained by fault growth initiating and propagating through dilatational kin-

ematics (Ferrill and Morris, 2003), or as vertically segmented fault zones that were controlled by the mechanically stratified nature of the country rock (i.e., DMG, Smye et al., 2021a), thus generating a series of vertically segmented fault segments that are below seismic resolution and imaged as high-angled fault zones at seismic resolution.

These faults are generally decoupled from the basin-compartmentalizing basement-rooted faults; however, the vertical section between basement-rooted and shallow faults diminishes along the margins of the basin, specifically, at the western margin of the basin as it transitions to the Diablo platform, and along the eastern margin of the Delaware Basin, where the presence of basement-rooted faults is observed to have some impact on the placement, orientation, and deformation of shallow faults near the western margin of the Central Basin platform (e.g., Figure 14).

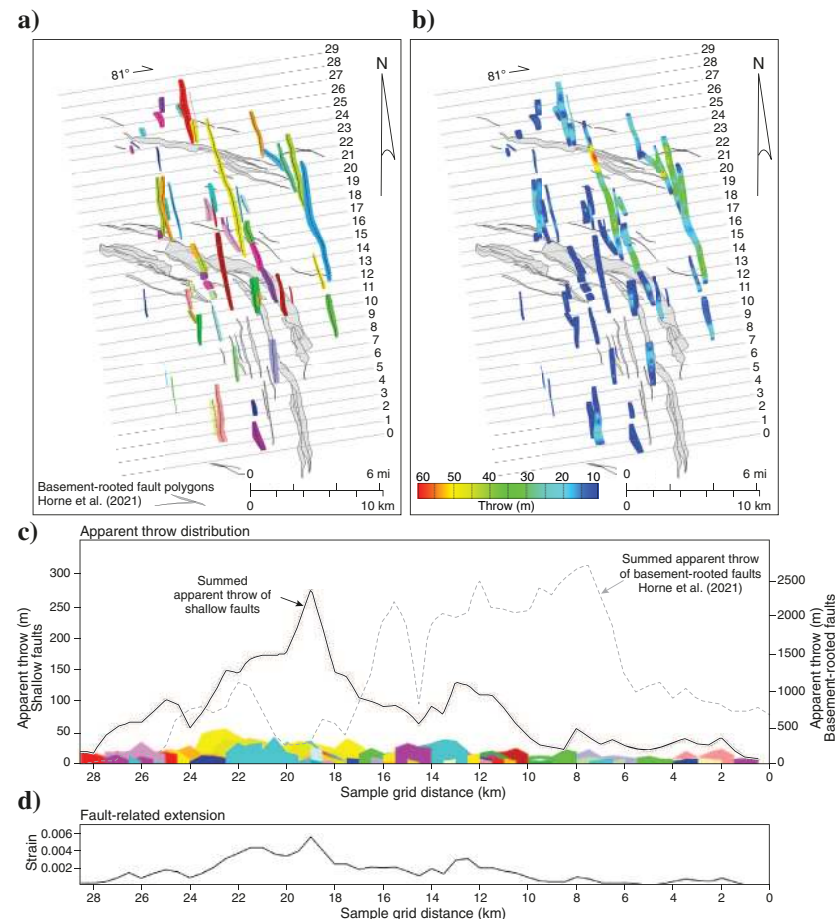


Figure 14. Fault array summation and strain diagrams for 3Db Waha-Lockridge. (a) Map view of shallow fault surfaces and 1 km sample grids. (b) Fault surfaces colored according to throw. Gray polygons shown in (a and b) represent basement-rooted fault polygons, which highlight horizontal shortening (heave) at the top ELBG (Horne et al., 2021). (c) Apparent throw distribution values are plotted as solid colors according to intersecting fault. The solid black line represents the summed apparent throw of shallow faults, and the dashed gray line represents the summed throw of basement-rooted faults mapped by Horne et al. (2021) within the 3Db Waha-Lockridge data set. (d) Fault-related extension.

Application to seismicity hazard assessment

Evidence for neotectonic reactivation

Triggered earthquake events increased significantly from 2010 to 2021 in the Delaware Basin, similar to other prominent petroleum basins in the central United States (Ellsworth, 2013). Given that the earthquake depths exhibit large uncertainty (mean depth uncertainty of 3.6 km [approximately 11,800 ft]), definitively associating earthquakes to specific faults is difficult. However, most M_L 2.0+ earthquakes mapped within the core seismogenic zone of the Delaware Basin are associated spatially with the newly presented shallow fault system. We adapt one of the provisional conclusions made by Horne et al. (2021), which states that many of the larger earthquakes have occurred on preexisting faults or in neighboring zones of deformation. This provisional conclusion can be tested by integrating 3D fault geometry, fault stress analysis, and earthquake hypocenters once the uncertainty in hypocentral location has been satisfactorily reduced.

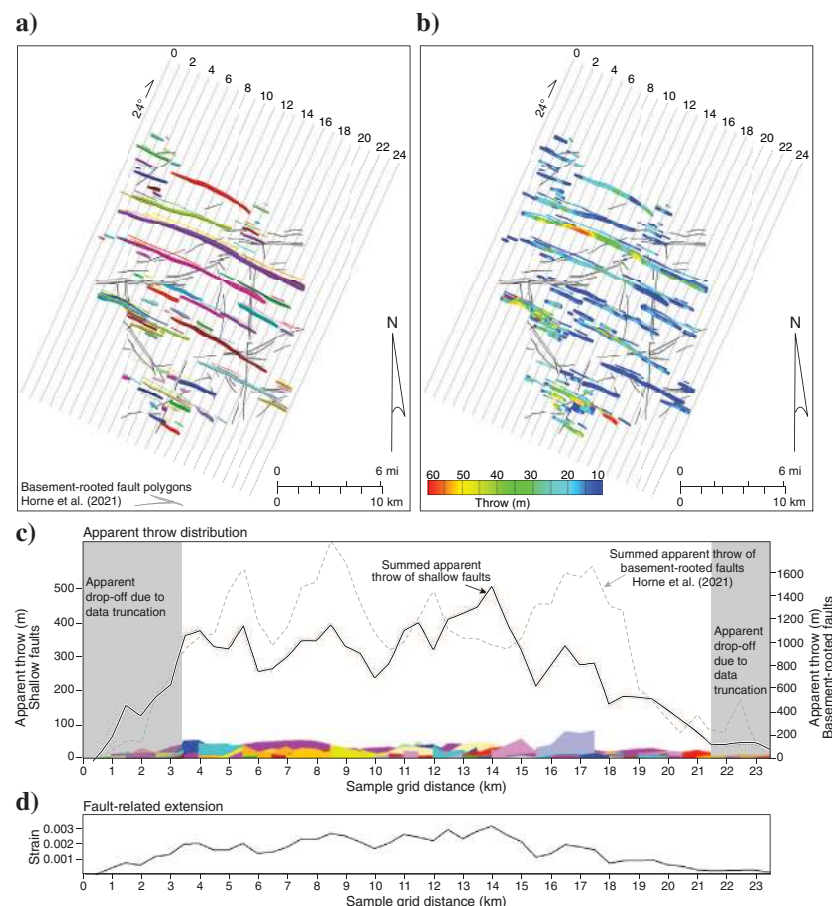


Figure 15. Fault array summation and strain diagrams for 3Dc Reeves County. (a) Fault and 1 km spaced vertical sample profiles are shown. (b) Fault-segment surfaces colored according to throw. Gray polygons shown in (a and b) represent basement-rooted fault polygons, which highlight horizontal displacement (heave) mapped at the top ELBG (Horne et al., 2021). (c) Apparent throw distribution values are plotted as solid colors according to intersecting fault. The solid black line represents the summed apparent throw of shallow faults at each intersecting sample trace and the dashed gray line represents the summed throw of basement-rooted faults mapped by Horne et al. (2021). (d) Fault-related extension (strain) also is the plot.

The causative hazard for preexisting faults reactivating is dependent on several factors, including fault orientation, mechanical stratigraphy, and geomechanical characteristics, and is further influenced by local and regional variations in principal stresses that can change with the azimuth of $S_{H\max}$. Understanding the relationship between faults and stress state is critical for providing predictive context for the analysis of earthquakes. Research completed by Morris et al. (2021), Smye et al. (2021b), and Dvory and Zoback (2021) has enhanced our understanding of regional and local variations in the stress field, and recent work completed by Hennings et al. (2021) has leveraged this information along with multiple earthquake catalogs, an assortment of geomechanical parameters, and fault segments interpretations in fault-slip analysis to establish the stability of fault segments under present conditions and determine the change in pore pressure (ΔP_p) needed to push fault segments to criticality.

The present-day stress regime of the Delaware Basin is extensional (Lund Snee and Zoback, 2018, 2020; Dvory and Zoback, 2021; Morris et al., 2021) and the regional stress state is likely influenced by the basement-rooted fault system that formed with the basin during the late-Paleozoic collisional events (e.g., Lund Snee and Zoback, 2018) and reflects the stress state of post-Permian tectonism (Zoback and Zoback, 1980, 1989; Horak, 1985; Ricketts et al., 2014; Lund Snee and Zoback, 2016, 2018, 2020; Dvory and Zoback, 2021). These events influenced the modern landscape and have been attributed to heterogeneities in the principal stress orientation $S_{H\max}$ and the in-situ stress of the Delaware Basin.

The azimuth of maximum horizontal stress $S_{H\max}$ systematically rotates counterclockwise from north-northwest trending in the south to northwest and west trending in the central parts of the basin, and east-northeast trending in the Culberson-Mentone earthquake zone north of the GFZ (Figure 16; Lund Snee and Zoback, 2018, 2020; Dvory and Zoback, 2021). Horne et al. (2021) suggest that the GFZ and first-order basement-rooted faults that bound the western margin of the Central Basin platform potentially influence the azimuth of $S_{H\max}$ regionally (Figure 16).

Characterization of seismogenic faults

Given that we use well-located earthquakes to assist with fault mapping, we have conducted a qualitative aerial assessment to determine which faults have recently slipped and have qualita-

tively classified segments as seismogenic, aseismogenic, or not associated with recent seismicity (Figure 17). Fault segments that are proximal to HypoDD relocated earthquake events are considered as recently seismogenic. Of the 421 faults mapped, 270 have been recently seismogenic and 151 have not. Furthermore, 173 faults have produced InSAR surface displacements and 248 have not. Of the faults with an interpreted surficial expression, 105 segments are associated with seismicity, and 68 are not associated with recent seismicity. We interpret these 68 faults with surficial expression and no association with seismicity to be rupturing aseismically. The seismogenic association of shallow faults in the Delaware Basin is illustrated (Figure 17) and tabulated (Table 4) to highlight these qualifications across each data region. From this analysis, we conclude that most mapped faults (approximately 65%) have been recently seismogenic and roughly 40% have displaced the ground surface.

Sampling bias and data impact

This mapped region extends over a significant portion of the Delaware Basin and, although high-resolution data sets are spatially limited, our integrated data sets enable the interpretation of shallow faults to be mapped at a semiregular sampling interval. The most trusted data sets cover approximately 1900 km² (approximately 8%) of the total area (Table 1). In these regions, we are confident that faults with trace lengths greater than approximately 0.5 km have been identified; however, these interpretations are limited to the upper-Permian age strata. Data regions with lower resolution, including 2D inset regions and the entirety of the seismogenic region of the Delaware Basin, have fault control information that often is interpolated laterally across significant distances. For these areas, we are confident that faults with trace lengths of greater than 4 km have been accounted for.

Fault segments are generally longer in regions controlled by sparse data sets; however, even fault segments

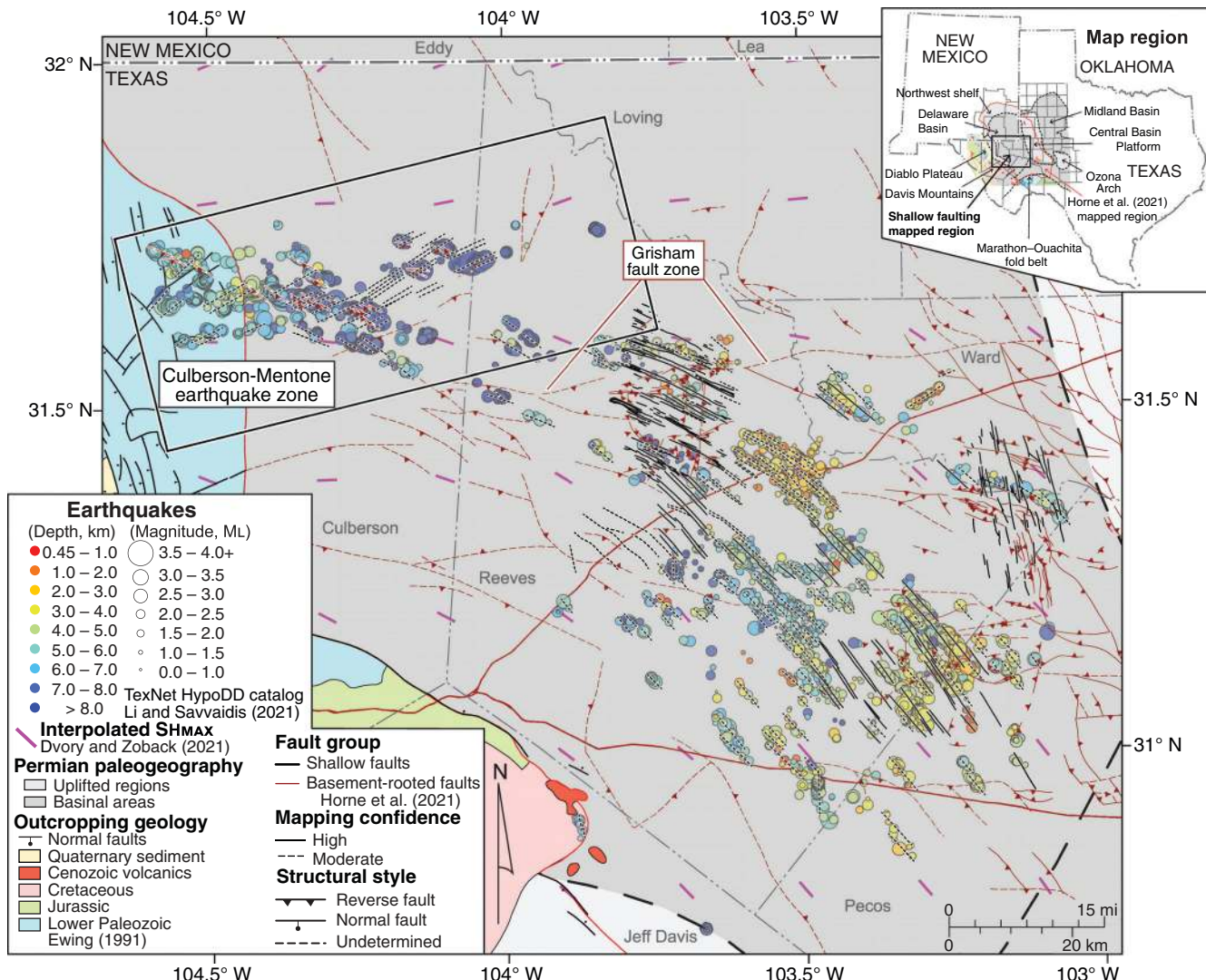


Figure 16. Map of the central Delaware basin showing newly mapped shallow fault interpretations and basement-rooted fault traces from Horne et al. (2021). Earthquake relative relocations from P. Li and A. Savvaidis (personal communication, 2021), hypocentral locations are sized by the magnitude and colored by the depth of the relocated event.

mapped using 3D seismic data are long relative to their observed vertical displacement (e.g., Schultz et al., 2008). This underdisplacement may be a product of data resolution, and faults are more likely composed of many hard- or soft-linked fault segments. Similarly, the oversteepened mapped and modeled nature of these fault segments may be the product of vertically segmented, and laterally staggered series of shallow faults and fractures, which are the product of the vertically variable mechanical properties of the country rock and are below data resolution.

Future applications

This characterization of shallow faults in the Delaware Basin can be combined with dynamic models of the DMG as subject to injection of oilfield wastewater. Ge et al. (2022) provide a regional analysis of

pore-pressure change in the DMG using the comprehensive geologic model of Smye et al. (2021a). They show that magnitudes of recent pore-pressure change range from 100 to 400+ psi (0.7–2.8 MPa). This change in pressure is undoubtedly sufficient to produce dynamic changes in the reservoir including fracturing and faulting. Seismic and aseismic fault-slip history can be compared with rates of pore-pressure change to determine fault instability thresholds. Our fault interpretation can be used to further guide the parameterization of these dynamic models including the implementation of fault-controlled permeability heterogeneity and anisotropy. The fault interpretation can be used to assess how injected fluids migrate laterally, potentially causing increases in water cuts for wells that produce hydrocarbons from the DMG. Given that some of the faults may extend downward into hydrocarbon-productive shales,

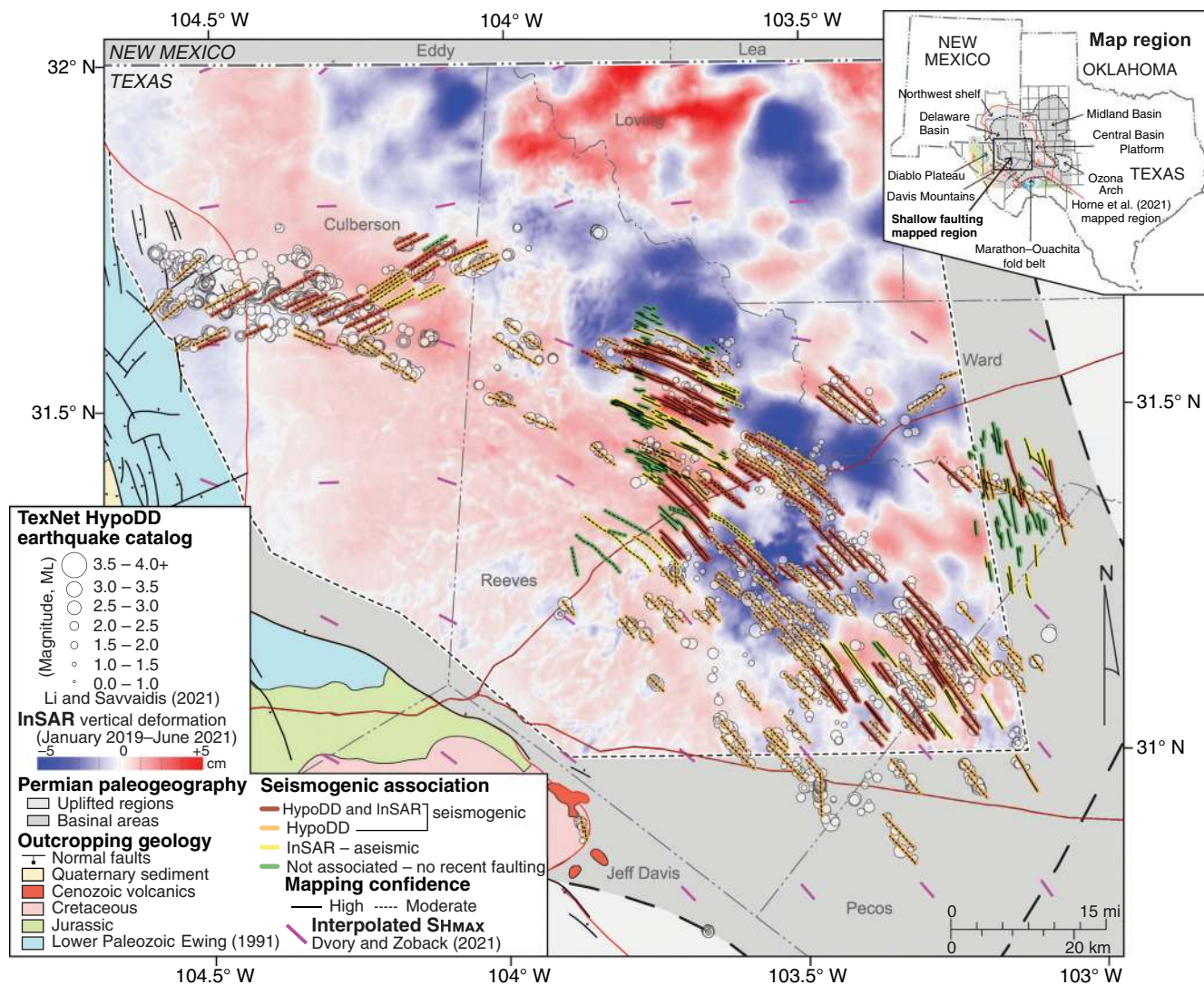


Figure 17. Seismogenic association of shallow faults in the Delaware Basin. Earthquake relative relocations from P. Li and A. Savvaidis (personal communication, 2021), are shown. Earthquake hypocentral locations are sized by magnitude. Shallow faults that are proximal to earthquakes are outlined in orange. Seismogenic faults that also are associated with InSAR surface deformation features are outlined in dark red. Fault segments that are associated only with InSAR observations are outlined in yellow. Segments that are not associated with recent seismicity or surface deformation are highlighted in green.

Table 4. Seismogenic association of shallow faults mapped within each interpretation domain.

Data region color and name	All faults #	EQ faults #	HypoDD		InSAR		Seismogenic		InSAR only	Not associated with seismicity
			Yes #	No #	Yes #	No #	InSAR + HypoDD	HypoDD only		
3Da	36	24	24	12	32	4	21	3	11	1
3Db	60	17	17	43	12	48	2	15	10	33
3Dc	115	40	40	73	56	57	22	18	34	39
2Da	14	11	11	3	9	5	9	2	0	3
2Db	31	24	24	7	23	8	17	7	6	1
2Dc	17	6	6	11	11	6	6	0	5	6
2Dd	11	9	9	2	11	0	9	0	2	0
InSAR and HypoDD EQ	19	19	19	0	19	0	19	0	0	0
HypoDD EQ Catalog	120	120	120	0	0	120	0	120	0	0
Faults used in analysis	421	270	270	151	173	248	105	165	68	83

this fault interpretation, along with previous work on basement-rooted faults, can be used to assess structural controls on hydrocarbons in place, gas/oil ratios, degree of overpressure, and presence of H₂S. Given that many of the faults extend upward into the overlying evaporites, the interpretation can be used to assess geologic to recent patterns of dissolution. Our interpretation also can be used to investigate the hazard of the seismogenic faults by thoroughly integrating fault moment analyses along with fault-slip history. Petroleum regulators can adopt this interpretation, with caveats regarding its confidence and completeness, for use in regulating petroleum operations.

Conclusion

The Delaware Basin of West Texas and southeast New Mexico is appreciably faulted and has experienced an increase in seismic activity, with earthquakes occurring in spatiotemporally isolated and diffuse clusters that are generally restricted to the central Delaware Basin. Many of these events have been linked to oilfield operations such as HF and wastewater disposal wastewater at multiple subsurface levels, and there are two distinct levels of faulting in the central region of the basin that exhibits the highest earthquake rate. These fault systems include a contractional basement-rooted fault system and a shallow extensional fault system.

Shallow faults are mapped across the seismogenic region of the south-central Delaware Basin, the trend of these segments follows rotations in the maximum horizontal stress, deformation accommodated along these high-angle fault segments is subtle, and the faults

are under displaced relative to their mapped lengths. Shallow faults are observed to be vertically decoupled from the basement-rooted faults; however, there may be subseismic fracture corridors that may occupy the vertical section between basement-rooted faults and shallow faults, as well as extending to the ground surface, as illuminated through the InSAR surface deformation map.

The shallow fault system is composed of the northwest–southeast-striking parallel trending segments, with a mean strike orientation of 310°, and dips that range ±15° from 70°. Faults range in length from 0.45 to 19.5 km and delineate a series of elongate, narrow graben, with a cumulative mapped length of >2000 km. These narrow elongate graben features are most reliably observed using 3D seismic reflection data; however, these features also have been interpreted by delineating patterns from InSAR observations and earthquake hypocentral locations from TexNet HypoDD relocated catalogs.

Fault lengths are generally consistent across data sets; however, faults mapped using sparse data sources are slightly longer than those interpreted using high-resolution data sources. The 3D seismic reflection data sets also illuminate variations in fault segment surface geometries that may be present across the mapped region. These geometries help inform fault modeling fault segments mapped from sparse regional data sets. Vertical deformation is only calculated in regions of sufficient data density, including 3Db Waha-Lockridge and 3Dc Reeves County 3D seismic surveys. In these regions, the magnitude of fault throw ranges from approximately 10 to 90 m. Fault attribute interrelationship analyses were conducted on interpretations from these 3D seismic data sets. These analyses show that the shallow faults interpreted in the 3Db (Waha-Lockridge) have the largest magnitude fault-related extensional strain in areas not overlying basement deformation. Conversely, shallow faults mapped within the 3Dc (Reeves County) data region have a more homogeneous deformation intensity that does not seem to be impacted by deformation observed within the basement-rooted fault system.

Deformation offset is mapped conservatively and has only been measured in terms of dip-slip movement in data regions supported by 3D seismic reflection surveys. In contrast to the basin-compartmentalizing contractile basement-rooted fault system, statistical analysis of fault length and throw shows that shallow faults have small throw given their mapped length producing a mean and highly anomalous TL ratio of 1:1000. The combination of steep dipping and underdisplaced fault segments could indicate that these features are strike slip in origin;

however, given the data available for integration, there is no observed or resolved amount of shear stress in the lateral direction or significant fault-fault interactions that would suggest development under a strike-slip or transtensional stress state.

Our interpretation that these faults are extensional rather than strike-slip transtensional is supported by data recently published by [Lund Snee and Zoback \(2022\)](#). Specifically, their maps show that the present-day faulting regime of the south-central Delaware Basin is currently normal, with A_{ϕ} values ranging from 0.5 to 0.75, well within the bounds of normal faulting (0.5 = normal, 1.5 = strike slip, and 2.5 = reverse). Furthermore, earthquake moment solutions compiled throughout literature and published by [Lund Snee and Zoback \(2022\)](#) show that, although there are some variabilities across the basin, moment-tensor solutions are dominantly normal. In addition, strike-slip deformation is a kinematic condition that would be coupled through the crust, impacting the full section of the basin. Given the data available to us, we do not find sufficient evidence of this coupling or interaction between these shallow features being linked to deformation in the deeper intervals. These fault segment surfaces are limited to the upper-Permian units and are decoupled from basement-rooted contractile features. These faults likely tip out as parallel-trending, mechanically stratified fracture corridors above and below these mapped systems, notably as shallow as creating surface ruptures or as deep as the Wolfcamp Formation. Increased access to higher resolution data sets (i.e., 3D seismic data) basinwide would certainly provide clarity to the kinematic development of these atypical fault zones.

Results from this work show that many recent earthquake sequences are associated with these faults in the south-central earthquake region of the Delaware Basin and InSAR observations show that these faults may be slipping aseismically. Future earthquakes can be compared spatially to this interpretation for structural context. The 3D faulted frameworks generated in 3Db Wahalockridge and 3Dc Reeves County interpretation regions can be used as foundations for mechanical analysis of fault rupture and seismogenesis. Finally, these faults can be used regionally or locally as controls for modifying permeability inputs to pore pressure modeling and fault rupture causation pathways and to generate discrete fracture network models as input to hydrogeologic models to better forecast future seismogenic hazards.

Data and materials availability

The fault interpretation and characterization were performed by integrating published data, publicly available data, well data as interpreted from the IHS Markit database under an academic license, and fault data from proprietary 3D seismic reflection data as interpreted or verified by the authors. Regional fault segments were mapped using map and cross-section interpretations and data publicly available from the RRC of Texas. Faults in the 3Da data region were provided by petro-

leum operators using proprietary seismic data and were verified by the authors. Faults within 3Db were interpreted by the authors on the basis of the Waha-Lockridge 3D seismic data set that can be obtained at <https://store.beg.utexas.edu/seminars-and-workshops/1312-sw0008.html> (last accessed January 2022). Faults in 3Dc were interpreted by the authors using proprietary seismic data sets provided by petroleum operators. A geographic information system shapefile and layer file for the subsurface fault trace interpretations derived by 2D mapping and 3D interpretations are publicly available within the Texas Data Repository at doi: [10.18738/T8/UHWLDR](https://doi.org/10.18738/T8/UHWLDR) (uploaded 10 January 2022). The TexNet earthquake catalog is available at <https://www.beg.utexas.edu/texnet-cisr/texnet/earthquake-catalog> (last accessed January 2022). The HypoDD relocated TexNet earthquake catalog is the product of an unpublished manuscript by P. Li and A. Savvaidis and is available at doi: [10.18738/T8/RBEGTH](https://doi.org/10.18738/T8/RBEGTH). The earthquake catalog for New Mexico can be accessed at the New Mexico Tech Seismological Observatory and is available at <https://geoinfo.nmt.edu/nmtdso/events/home.cfm> (last accessed January 2022). The U.S. Geological Survey Advanced National Seismic System Comprehensive Catalog (ComCat) is available at <https://earthquake.usgs.gov/earthquakes/search/> (last accessed January 2022).

Acknowledgments

We thank XTO and ExxonMobil for access to proprietary fault information. We thank TGS for access to proprietary seismic data. We thank Cimarex Energy Co. for advice on fault mapping. We thank IHS Markit for access to well databases, Schlumberger for access to the Petrel E&P Software Platform, Badley Geoscience Ltd. for access to T7 software, and Petroleum Experts for access to MOVE software. The authors thank A. Afifi, D. Lankford-Bravo, two anonymous reviewers, and the associate editor B. Wallet for feedback and suggestions that greatly enhanced the manuscript. This work was supported by the State of Texas through The University of Texas Bureau of Economic Geology (BEG) TexNet Seismic Monitoring and Research Project and the industrial associates of the Center for Integrated Seismicity Research (CISR). J. Chen and S. Staniewicz were supported by the NASA Earth Surface and Interior Program, grant 80NSSC18K0467.

References

- Adams, D. C., and G. R. Keller, 1996, Precambrian basement geology of the Permian Basin region of West Texas and eastern New Mexico: A geophysical perspective: AAPG Bulletin, **80**, 410–431, doi: [10.1306/64ED87FA-1724-11D7-8645000102C1865D](https://doi.org/10.1306/64ED87FA-1724-11D7-8645000102C1865D).
- Adams, J. E., H. N. Frenzel, M. L. Rhodes, and D. P. Johnson, 1951, Starved Pennsylvanian Midland Basin: AAPG Bulletin, **35**, 2600–2607.
- Anderson, E. M., 1951, The dynamics of faulting and dyke formation with applications to Brittan: Oliver and Boyd.

- Brown, A., 2019, Post-Permian history of the greater Permian Basin area, in S. C. Ruppel, ed., Anatomy of a Paleozoic Basin: The Permian Basin, USA (vol. 1): The University of Texas at Austin, Bureau of Economic Geology Report of Investigations 285; AAPG Memoir 118, 97–134.
- Budnik, R. T., 1986, Left-lateral intraplate deformation along the ancestral rocky mountains: Implications for late Paleozoic plate motions: Tectonophysics, **132**, 195–214, doi: [10.1016/0040-1951\(86\)90032-6](https://doi.org/10.1016/0040-1951(86)90032-6).
- Charzynski, K., K. Faith, Z. Fenton, A. Shedeed, M. McKee, S. Bjorlie, and M. Richardson, 2019, Delaware basin horizontal Wolfcamp case study: Mitigating H₂S and excessive water production through isolating densely fractured intervals correlative to seismically mapped shallow graben features in the Delaware Mountain Group: Unconventional Resources Technology Conference, SEG, Global Meeting Abstracts, 4126–4141, doi: [10.15530/urtec-2019-1037](https://doi.org/10.15530/urtec-2019-1037).
- Comer, J. B., 1991, Stratigraphic analysis of the upper Devonian Woodford Formation, Permian Basin, West Texas and Southeastern New Mexico: Bureau of Economic Geology, The University of Texas at Austin.
- Cook, S., M. McKee, and S. Bjorlie, 2019, Delaware Basin horizontal Wolfcamp case history: HTI fracture analysis to avoid H₂S and extraneous water linked to graben features: Unconventional Resources Technology Conference, SEG, Global Meeting Abstracts, 188–202, doi: [10.15530/urtec-2019-452](https://doi.org/10.15530/urtec-2019-452).
- Cowie, P. A., and C. H. Scholz, 1992, Displacement-length scaling relationship for faults: Data synthesis and discussion: Journal of Structural Geology, **14**, 1149–1156, doi: [10.1016/0191-8141\(92\)90066-6](https://doi.org/10.1016/0191-8141(92)90066-6).
- Davis, B. R., and S. Mosher, 2015, Complex structural and fluid flow evolution along the Grenville Front, west Texas: Geosphere, **11**, 868–898, doi: [10.1130/GES01098.1](https://doi.org/10.1130/GES01098.1).
- Dickinson, W. R., and T. F. Lawton, 2003, Sequential intercontinental suturing as the ultimate control for Pennsylvanian Ancestral Rocky Mountains deformation: Geology, **31**, 609–612, doi: [10.1130/0091-7613\(2003\)031<0609:SISATU>2.0.CO;2](https://doi.org/10.1130/0091-7613(2003)031<0609:SISATU>2.0.CO;2).
- Denison, R. E., W. H. J. Burke, E. A. Hetherington, and J. B. Otto, 1971, Basement rock framework of parts of Texas, southern New Mexico and northern Mexico, in K. Seewald and D. Sundeen, eds., The geologic framework of the Chihuahua tectonic belt: West Texas Geological Society Publication, 71–59.
- Dvory, N. Z., and M. D. Zoback, 2021, Prior oil and gas production can limit the occurrence of injection-induced seismicity: A case study in the Delaware Basin of western Texas and southeastern New Mexico, USA: Geology, **49**, 1198–1203, doi: [10.1130/G49015.1](https://doi.org/10.1130/G49015.1).
- Ellsworth, W. L., 2013, Injection-induced earthquakes: Science, **341**, 1225942, doi: [10.1126/science.1225942](https://doi.org/10.1126/science.1225942).
- Energy Information Administration (EIA), 2018, Permian Basin Wolfcamp Shale Play geology review, U.S. Energy Inf. Adm. Rep, available at <https://www.eia.gov/maps/>pdf/PermianBasin_Wolfcamp_EIAReport_Oct2018.pdf, accessed 3 January 2022.
- Energy Information Administration (EIA), 2020, Permian Basin: Wolfcamp, Bone Spring, Delaware Shale Plays of the Delaware Basin, U.S. Energy Inf. Adm. Rep, available at https://www.eia.gov/maps/pdf/Permian_WolfCamp_BoneSpring_Delaware_EIA_Report_Feb2020.pdf, accessed 3 January 2022.
- Energy Information Administration (EIA), 2021, Permian region, Drill. Product. Rep, available at <https://www.eia.gov/petroleum/drilling/pdf/permian.pdf>, accessed 3 January 2022.
- Ewing, T. E., 1991, The tectonic framework of Texas: Text to accompany “The Tectonic Map of Texas”: Bureau of Economic Geology, the University of Texas at Austin.
- Ewing, T. E., 2015, Extended abstract: Insights from the Texas through time project: Gulf Coast Association of Geological Societies Transactions, **65**, 447–453.
- Ewing, T. E., 2019, Tectonics of the West Texas (Permian) Basin — Origins, structural geology, subsidence, and later modification, in S. C. Ruppel, ed., Anatomy of a Paleozoic Basin: The Permian Basin, USA (vol. 1): The University of Texas at Austin, Bureau of Economic Geology Report of Investigations 285; AAPG Memoir 118, 63–96.
- Ewing, T. E., M. A. Barnes, and R. E. Denison, 2019, Proterozoic foundations of the Permian Basin, West Texas and Southeastern New Mexico — A review, in S. C. Ruppel, ed., Anatomy of a Paleozoic Basin: The Permian Basin, USA (vol. 1): The University of Texas at Austin, Bureau of Economic Geology Report of Investigations 285; AAPG Memoir 118, 43–61.
- Fairhurst, B., T. Ewing, and B. Lindsay, 2021, West Texas (Permian) Super Basin, United States: Tectonics, structural development, sedimentation, petroleum systems, and hydrocarbon reserves: AAPG Bulletin, **105**, 1099–1147, doi: [10.1306/03042120130](https://doi.org/10.1306/03042120130).
- Ferrill, D. A., and A. P. Morris, 2003, Dilational normal faults: Journal of Structural Geology, **25**, 183–196, doi: [10.1016/S0191-8141\(02\)00029-9](https://doi.org/10.1016/S0191-8141(02)00029-9).
- Ferrill, D. A., A. P. Morris, R. N. McGinnis, K. J. Smart, S. S. Wigginton, and N. J. Hill, 2017, Mechanical stratigraphy and normal faulting: Journal of Structural Geology, **94**, 275–302, doi: [10.1016/j.jsg.2016.11.010](https://doi.org/10.1016/j.jsg.2016.11.010).
- Flawn, P. T., 1956, Basement rocks of Texas and Southeast New Mexico: The University of Texas at Austin, Bureau of Economic Geology.
- Frenzel, H. N., R. R. Bloomer, R. B. Cline, J. M. Cys, J. E. Galley, W. R. Gibson, J. M. Hills, W. E. King, W. R. Seager, F. E. Kottlowski, S. Thompson, III, G. C. Luff, B. T. Pearson, and D. C. van Siclen, 1988, The Permian Basin region, in L. L. Sloss, ed., Sedimentary cover — North American Craton U.S., D-2: Geological Society of America, 261–306.
- Frohlich, C., H. de Shon, B. Stump, C. Hayward, M. Hornbach, and J. I. Walter, 2016, A historical review of induced earthquakes in Texas: Seismological Research Letters, **87**, 1022–1038, doi: [10.1785/0220160016](https://doi.org/10.1785/0220160016).

- Frohlich, C., C. Hayward, J. Rosenblit, C. Aiken, P. Hennings, A. Savvaidis, C. Lemons, E. Horne, J. I. Walter, and H. R. DeShon, 2020, Onset and cause of increased seismic activity near Pecos, West Texas, United States, from observations at the Lajitas TXAR seismic array: *Journal of Geophysical Research: Solid Earth*, **125**, e2019JB017737, doi: [10.1029/2019JB017737](https://doi.org/10.1029/2019JB017737).
- Fu, Q., R. W. Baumgardner, Jr., and H. S. Hamlin, 2020, Early Permian (Wolfcampian) succession in the Permian Basin: Icehouse platform, slope carbonates, and basinal mudrocks, in S. C. Ruppel, ed., *Anatomy of a Paleozoic basin: The Permian Basin, USA*: The University of Texas at Austin, Bureau of Economic Geology Report of Investigations 285 and AAPG Memoir 118, 185–225.
- Galley, J. E., 1958, Oil and geology in the Permian Basin of Texas and New Mexico, in L. G. Weeks, ed., *Habitat of oil*: AAPG, 125, 395–446.
- Gardiner, W. B., 1990, Fault fabric and structural subprovinces of the Central Basin platform: A model for strike-slip movement, in J. E. Flis and R. C. Price, eds., *Permian Basin oil and gas fields: Innovative ideas in exploration and development*: West Texas Geological Society, Publication 90.87, 15–27.
- Gardner, M. H., 1992, Sequence stratigraphy of eolian-derived turbidites: Deep water sedimentation patterns along an arid carbonate platform and their impact on hydrocarbon recovery in Delaware Mountain Group reservoirs, West Texas, in D. H. Mruk and B. C. Curran, eds., *Permian Basin exploration and production strategies: Applications of sequence stratigraphic and reservoir characterization concepts*: West Texas Geological Society, Publication 92.91, 7–11.
- Ge, J., J.-P. Nicot, K. M. Smye, S. A. Hosseini, S. Gao, and C. L. Breton, 2022, Recent water disposal and pore pressure evolution in the Delaware Mountain Group, Delaware Basin, Southeast New Mexico and West Texas: *Journal of Hydrology: Regional Studies*, **40**, 101041, doi: [10.1016/j.ejrh.2022.101041](https://doi.org/10.1016/j.ejrh.2022.101041).
- Grigoratos, I., A. Savvaidis, and E. Rathje, 2022, Distinguishing the causal factors of induced seismicity in the Delaware Basin: Hydraulic fracturing or wastewater disposal? *Seismological Research Letters*, doi: [10.1785/0220210320](https://doi.org/10.1785/0220210320).
- Gudmundsson, A., G. De Guidi, and S. Scudero, 2013, Length-displacement scaling and fault growth: *Tectonophysics*, **608**, 1298–1309, doi: [10.1016/j.tecto.2013.06.012](https://doi.org/10.1016/j.tecto.2013.06.012).
- Hardage, B. A., 2015, Pitfall experiences when interpreting complex structure with low-quality seismic images: *Interpretation*, **3**, no. 1, SB29–SB37, doi: [10.1190/INT-2014-0118.1](https://doi.org/10.1190/INT-2014-0118.1).
- Hardage, B. A., and R. P. Major, 1998, Integrated strategies for carbonate reservoir reserve growth: An example from the Ellenburger Group, Permian Basin, West Texas: National Energy Technology Laboratory.
- Hardage, B. A., V. M. Pendleton, R. P. Major, G. B. Asquith, D. Schultz-Ela, and D. E. Lancaster, 1999, Using petrophysics and cross-section balancing to interpret complex structure in a limited-quality 3-D seismic image: *Geophysics*, **64**, 1760–1773, doi: [10.1190/1.1444682](https://doi.org/10.1190/1.1444682).
- Haruna, K. A., O. J. Ojo, and W. Odufisan, 2014, Subsurface mapping and reservoir evaluation of West Waha and Worsham-Bayer field area of southeastern Delaware Basin, West Texas: *The Pacific Journal of Science and Technology*, **15**, 360–374.
- Hennings, P., N. Dvory, E. Horne, P. Li, A. Savvaidis, and M. Zoback, 2021, Stability of the fault systems that host-induced earthquakes in the Delaware Basin of West Texas and Southeast New Mexico: *The Seismic Record*, **1**, 96–106, doi: [10.1785/0320210020](https://doi.org/10.1785/0320210020).
- Hennings, P. H., 1994, Structural transect of the southern Chihuahua Fold Belt between Ojinaga and Aldama, Chihuahua, Mexico: *Tectonics*, **13**, 1445–1460, doi: [10.1029/94TC00800](https://doi.org/10.1029/94TC00800).
- Hennings, P. H., J. Lund Snee, J. L. Osmond, H. R. DeShon, R. Dommis, E. Horne, C. Lemons, M. D. Zoback, J. E. L. Snee, J. L. Osmond, H. R. DeShon, R. Dommis, E. Horne, C. Lemons, and M. D. Zoback, 2019, Injection-induced seismicity and fault-slip potential in the Fort Worth Basin, Texas: *Bulletin of the Seismological Society of America*, **109**, 1615–1634, doi: [10.1785/0120190017](https://doi.org/10.1785/0120190017).
- Hentz, T. F., and C. D. Henry, 1989, Evaporite-hosted native sulfur in Trans-Pecos Texas: Relations to late-phase Basin and range deformation: *Geology*, **17**, 400, doi: [10.1130/0091-7613\(1989\)017<0400:EHNSIT>2.3.CO;2](https://doi.org/10.1130/0091-7613(1989)017<0400:EHNSIT>2.3.CO;2).
- Henry, C. D., J. K. Gluck, N. T. Bockoven, and J. G. Price, 1985, Summary of the tectonic development of Trans-Pecos Texas: The University of Texas at Austin, Bureau of Economic Geology.
- Henry, C. D., and J. G. Price, 1986, Early basin and range development in Trans-Pecos Texas and adjacent Chihuahua: Magmatism and orientation, timing, and style of extension: *Journal of Geophysical Research: Solid Earth*, **91**, 6213–6224, doi: [10.1029/JB091iB06p06213](https://doi.org/10.1029/JB091iB06p06213).
- Hills, J. M., 1963, Late Paleozoic tectonics and mountain ranges, Western Texas to Southern Colorado: *AAPG Bulletin*, **47**, 360, doi: [10.1306/BC7439E5-16BE-11D7-8645000102C1865D](https://doi.org/10.1306/BC7439E5-16BE-11D7-8645000102C1865D).
- Hills, J. M., 1970, Late Paleozoic structural directions in southern Permian Basin, west Texas and southeastern New Mexico: *AAPG Bulletin*, **54**, 1809–1827, doi: [10.1306/5D25CC3B-16C1-11D7-8645000102C1865D](https://doi.org/10.1306/5D25CC3B-16C1-11D7-8645000102C1865D).
- Hills, J. M., 1984, Sedimentation, tectonism, and hydrocarbon generation in Delaware Basin, west Texas and southeastern New Mexico: *AAPG Bulletin*, **68**, 250–267, doi: [10.1306/AD460A08-16F7-11D7-8645000102C1865D](https://doi.org/10.1306/AD460A08-16F7-11D7-8645000102C1865D).
- Horak, R. L., 1985, Trans-Pecos tectonism and its effect on the Permian Basin, in P. W. Dickerson and W. R. Muehlberger, eds., *Structure and tectonics of Trans-Pecos Texas*, 85th–81st ed.: West Texas Geological Society, 81–87.
- Horne, E. A., P. H. Hennings, J. L. Osmond, and H. R. DeShon, 2020, Structural characterization of potentially seismogenic faults in the Fort Worth Basin: *Interpretation*, **8**, no. 2, T323–T347, doi: [10.1190/INT-2019-0188.1](https://doi.org/10.1190/INT-2019-0188.1).

- Horne, E. A., P. H. Hennings, and C. K. Zahm, 2021, Basement-rooted faults of the Delaware Basin and Central Basin platform, Permian Basin, west Texas and southeastern New Mexico, *in* O. A. Callahan and P. Eichhubl, eds., The geologic basement of Texas: A volume in honor of Peter T. Flawn: The University of Texas at Austin, Bureau of Economic Geology Report of Investigations No. 286.
- Horne, E. A., K. M. Smye, and P. H. Hennings, 2022, Structure and characteristics of the basement in the Fort Worth Basin, *in* O. A. Callahan and P. Eichhubl, eds., The geologic basement of Texas: A volume in honor of Peter T. Flawn: The University of Texas at Austin, Bureau of Economic Geology Report of Investigations No. 286.
- IHS Energy, 2009, GDS database: Unpublished Geological Data Services database available from IHS Energy, 15 Inverness Way East, Englewood, CO 80112.
- Kluth, C. F., 1998, Late Paleozoic deformation of interior North America: The Greater Ancestral Rocky Mountains: Discussion: AAPG Bulletin, **82**, 2272–2276, doi: [10.1306/00AA7F18-1730-11D7-8645000102C1865D](https://doi.org/10.1306/00AA7F18-1730-11D7-8645000102C1865D).
- Krantz, B., and T. Neely, 2016, Subsurface structural interpretation, *in* B. Krantz, C. Ormand, and B. Freeman, eds., 3-D structural interpretation: AAPG, 111, 91–109.
- Leary, R. J., P. Umhoefer, M. E. Smith, and N. Riggs, 2017, A three-sided orogen: A new tectonic model for Ancestral Rocky Mountain uplift and basin development: Geology, **45**, 399–402, doi: [10.1130/G38830.1](https://doi.org/10.1130/G38830.1).
- Lomax, A., and A. Savvaidis, 2019, Improving absolute earthquake location in west Texas using probabilistic, proxy ground-truth station corrections: Journal of Geophysical Research: Solid Earth, **124**, 11447–11465, doi: [10.1029/2019JB017727](https://doi.org/10.1029/2019JB017727).
- Lund, K., S. E. Box, C. Holm-Denoma, C. A. San Juan, R. J. Blakely, R. W. Saltus, E. D. Anderson, and E. H. Dewitt, 2015, Basement domain map of the conterminous United States and Alaska: U.S. Geological Survey.
- McConnell, D. A., 1989, Determination of offset across the northern margin of the Wichita uplift, southwest Oklahoma: Geological Society of America Bulletin, **101**, 1317–1332, doi: [10.1130/0016-7606\(1989\)101<1317:DOOATN>2.3.CO;2](https://doi.org/10.1130/0016-7606(1989)101<1317:DOOATN>2.3.CO;2).
- Lund Snee, J. E., and M. D. Zoback, 2016, State of stress in Texas: Implications for induced seismicity: Geophysical Research Letters, **43**, 10208–10214, doi: [10.1002/2016GL070974](https://doi.org/10.1002/2016GL070974).
- Lund Snee, J.-E., and M. D. Zoback, 2018, State of stress in the Permian Basin, Texas and New Mexico: Implications for induced seismicity: The Leading Edge, **37**, 127–134, doi: [10.1190/tle37020127.1](https://doi.org/10.1190/tle37020127.1).
- Lund Snee, J.-E., and M. D. Zoback, 2020, Multiscale variations of the crustal stress field throughout North America: Nature Communications, **11**, 1951, doi: [10.1038/s41467-020-15841-5](https://doi.org/10.1038/s41467-020-15841-5).
- Lund Snee, J.-E., and M. D. Zoback, 2022, State of stress in areas of active unconventional oil and gas development in North America: AAPG Bulletin, **106**, 355–385, doi: [10.1306/08102120151](https://doi.org/10.1306/08102120151).
- Mosher, S., 1998, Tectonic evolution of the southern Laurentian Grenville orogenic belt: Bulletin of the Geological Society of America, **110**, 1357–1375, doi: [10.1130/0016-7606\(1998\)110<1357:TEOTSL>2.3.CO;2](https://doi.org/10.1130/0016-7606(1998)110<1357:TEOTSL>2.3.CO;2).
- Morris, A. P., P. H. Hennings, E. A. Horne, and K. M. Smye, 2021, Stability of basement-rooted faults in the Delaware Basin of Texas and New Mexico, USA: Journal of Structural Geology, **149**, 104360, doi: [10.1016/j.jsg.2021.104360](https://doi.org/10.1016/j.jsg.2021.104360).
- Muehlberger, W. R., 1965, Late Paleozoic movement along the Texas Lineament: Transactions of the New York Academy of Sciences, **27**, 385–392, doi: [10.1111/j.2164-0947.1965.tb02976.x](https://doi.org/10.1111/j.2164-0947.1965.tb02976.x).
- Muehlberger, W. R., R. E. Denison, and E. G. Lidiak, 1967, Basement rocks in continental interior of United States: AAPG Bulletin, **51**, 2351–2380, doi: [10.1306/5D25C277-16C1-11D7-8645000102C1865D](https://doi.org/10.1306/5D25C277-16C1-11D7-8645000102C1865D).
- Nance, H. S., 2020, Upper Permian Delaware Mountain Group: Record of highstand/lowstand platform shedding, *in* S. Ruppel, ed., Anatomy of a Paleozoic Basin: The Permian Basin, vol. 2: Bureau of Economic Geology, Report of Investigations 285-2, 399–436.
- New Mexico Tech Seismological Observatory, 2021, Seismic events — New Mexico Tech seismological observatory, available at <https://geoinfo.nmt.edu/nmtso/events/home.cfml>, accessed 5 February 2021.
- Poole, F. G., W. J. Perry, R. J. Madrid, and R. Amaya-Martinez, 2005, Tectonic synthesis of the Ouachita-Marathon-Sonora orogenic margin of southern Laurentia: Stratigraphic and structural implications for timing of deformational events and plate-tectonic model: Geological Society of America, 393, 543–596.
- Railroad Commission of Texas, 2022, www.rrc.texas.gov, accessed August 2022.
- Ross, C. A., 1986, Paleozoic evolution of southern margin of Permian Basin: Geological Society of America Bulletin, **97**, 536–554, doi: [10.1130/0016-7606\(1986\)97<536:PEOSMO>2.0.CO;2](https://doi.org/10.1130/0016-7606(1986)97<536:PEOSMO>2.0.CO;2).
- Ricketts, J. W., K. E. Karlstrom, A. Priewisch, L. J. Crossey, V. J. Polyak, and Y. Asmerom, 2014, Quaternary extension in the Rio Grande rift at elevated strain rates recorded in travertine deposits, central New Mexico: Lithosphere, **6**, 3–16, doi: [10.1130/L278.1](https://doi.org/10.1130/L278.1).
- Rougvie, J. R., W. D. Carlson, P. Copeland, and J. N. Connelly, 1999, Late thermal evolution of Proterozoic rocks in the northeastern Llano Uplift, central Texas: Precambrian Research, **94**, 49–72, doi: [10.1016/S0301-9268\(98\)00103-X](https://doi.org/10.1016/S0301-9268(98)00103-X).
- Ruppel, S. C., 2019a, Anatomy of a Paleozoic Basin: The Permian Basin, USA: AAPG Memoir, 1, 412.
- Ruppel, S. C., 2019b, Introduction, overview, and evolution, *in* S. C. Ruppel, ed., Anatomy of a Paleozoic Basin: The Permian Basin, USA (vol. 1): The University of Texas at Austin, Bureau of Economic Geology Report of Investigations 285; AAPG Memoir 118, 1–27.
- Savvaidis, A., A. Lomax, and C. Breton, 2020, Induced seismicity in the Delaware Basin, West Texas, is caused

- by hydraulic fracturing and wastewater disposal: Bulletin of the Seismological Society of America, **110**, 2225–2241, doi: [10.1785/0120200087](https://doi.org/10.1785/0120200087).
- Savvaidis, A., B. Young, G.-C. D. Huang, and A. Lomax, 2019, TexNet: A statewide seismological network in Texas: Seismological Research Letters, **90**, 1702–1715, doi: [10.1785/0220180350](https://doi.org/10.1785/0220180350).
- Schultz, R. A., R. Soliva, H. Fossen, C. H. Okubo, and D. M. Reeves, 2008, Dependence of displacement-length scaling relations for fractures and deformation bands on the volumetric changes across them: Journal of Structural Geology, **30**, 1405–1411, doi: [10.1016/j.jsg.2008.08.001](https://doi.org/10.1016/j.jsg.2008.08.001).
- Shumaker, R. C., 1992, Paleozoic structure of the Central Basin uplift and adjacent Delaware Basin, west Texas: AAPG Bulletin, **76**, 1804–1824, doi: [10.1306/BDFF8AD8-1718-11D7-8645000102C1865D](https://doi.org/10.1306/BDFF8AD8-1718-11D7-8645000102C1865D).
- Silver, B. A., and R. G. Todd, 1969, Permian cyclic strata, northern Midland and Delaware Basins, west Texas and southeastern New Mexico: AAPG Bulletin, **53**, 2223–2251, doi: [10.1306/5D25C94D-16C1-11D7-8645000102C1865D](https://doi.org/10.1306/5D25C94D-16C1-11D7-8645000102C1865D).
- Skoumal, R. J., A. J. Barbour, M. R. Brudzinski, T. Langenkamp, and J. O. Kaven, 2020, Induced seismicity in the Delaware Basin, Texas: Journal of Geophysical Research: Solid Earth, **125**, e2019JB018558, doi: [10.1029/2019JB018558](https://doi.org/10.1029/2019JB018558).
- Smee, K., D. A. Banerji, R. Eastwood, G. McDaid, and P. Hennings, 2021a, Lithology and reservoir properties of the Delaware Mountain Group of the Delaware Basin and implications for saltwater disposal and induced seismicity: Journal of Sedimentary Research, **91**, 1113–1132, doi: [10.2110/jsr.2020.134](https://doi.org/10.2110/jsr.2020.134).
- Smee, K. M., P. H. Hennings, and E. A. Horne, 2021b, Variations in vertical stress in the Permian Basin region: AAPG Bulletin, **105**, 1893–1907, doi: [10.1306/10092019189](https://doi.org/10.1306/10092019189).
- Smee, K. M., C. R. Lemons, R. Eastwood, G. McDaid, and P. H. Hennings, 2019, Stratigraphic architecture and petrophysical characterization of formations for deep disposal in the Fort Worth Basin, Texas: Interpretation, **7**, no. 4, SL1–SL17, doi: [10.1190/INT-2018-0195.1](https://doi.org/10.1190/INT-2018-0195.1).
- Staniewicz, S., J. Chen, H. Lee, J. Olson, A. Savvaidis, R. Reedy, C. Breton, E. Rathje, and P. Hennings, 2020, InSAR reveals complex surface deformation patterns over an 80,000 km² oil-producing region in the Permian Basin: Geophysical Research Letters, **47**, e2020GL090151, doi: [10.1029/2020GL090151](https://doi.org/10.1029/2020GL090151).
- Tai, P.-C., and S. L. Dorobek, 2000, Tectonic model for late Paleozoic deformation of the Central Basin platform, Permian Basin region, west Texas, in W. D. DeMis, M. K. Nelis, and R. C. Trentham, eds., The Permian Basin: Proving ground for tomorrow's technologies: West Texas Geological Society, 157–176.
- TexNet, 2021, Texas seismological network earthquake catalog, available at <https://www.beg.utexas.edu/texnet-cisr/texnet/earthquake-catalog>, accessed 14 September 2021.
- TexNet Earthquake Catalog, 2022, <https://www.beg.utexas.edu/texnet-cisr/texnet/earthquake-catalog>, accessed August 2022.
- Tung, S., G. Zhai, and M. Shirzaei, 2020, Potential link between 2020 Mentone, West Texas M5 earthquake and nearby wastewater injection: Implications for aquifer mechanical properties: Geophysical Research Letters, **48**, e2020GL090551, doi: [10.1029/2020GL090551](https://doi.org/10.1029/2020GL090551).
- Walper, J. L., 1977, Paleozoic tectonics of the southern margin of North America: Transactions of the Gulf Coast Association of Geological Societies, **27**, 230–241.
- Walper, J. L., 1982, Plate tectonic evolution of the Fort Worth Basin, in C. A. Martin, ed., Petroleum geology of the Fort Worth Basin and bend arch area: Dallas Geological Society, 237–253.
- Wuellner, D. E., L. R. Lehtonen, and W. C. James, 1986, Sedimentary-tectonic development of the Marathon and Val Verde Basins, west Texas, USA: Permo-Carboniferous migrating foredeep, in P. A. Allen and P. Homewood, eds., Foreland Basins: Blackwell Publishing Ltd., 347–368.
- Yang, K.-M., and S. L. Dorobek, 1995, The Permian Basin of west Texas and New Mexico: Tectonic history of a “composite” foreland basin and its effects on stratigraphic development, in S. L. Dorobek and G. M. Ross, eds., Stratigraphic evolution of Foreland Basins: SEPM Special Publication No. 52, 149–174.
- Zoback, M. D., and S. M. Gorelick, 2012, Earthquake triggering and large-scale geologic storage of carbon dioxide: Proceedings of the National Academy of Sciences, **109**, 10164–10168, doi: [10.1073/pnas.1202473109](https://doi.org/10.1073/pnas.1202473109).
- Zoback, M. L., and M. Zoback, 1980, State of stress in the conterminous United States: Journal of Geophysical Research: Solid Earth, **85**, 6113–6156, doi: [10.1029/JB085iB11p06113](https://doi.org/10.1029/JB085iB11p06113).
- Zoback, M. L., and M. D. Zoback, 1989, Tectonic stress field of the continental United States, in L. C. Pakiser and W. D. Mooney, eds., Geophysical framework of the continental United States: Geological Society of America Memoir, 523–540.



Elizabeth Horne received a B.S. (2013) in geology from Utah State University and an M.S. (2016) in geology from Colorado School of Mines. She is a research scientist associate III at The University of Texas BEG where she is the structural interpretation specialist for the TexNet Seismic Monitoring and CISR consortium.

She also is the lead principal investigator for the Regional Induced Seismicity Collaborative. Her research interests include integrating field and subsurface data sets to generate 3D models that are used to better understand the kinematic evolution of various structural systems, as well as

assess seismic hazards, naturally occurring and induced. She is a member of several professional societies, including AAPG, AGU, GSA, and RMAG.



Peter Hennings received a B.S. (1983) and M.S. (1986) from Texas A&M University, and a Ph.D. (1991) from The University of Texas. He is a senior research scientist at The University of Texas BEG where he is a principal investigator for the CISR and a lecturer in the Department of Geological Sciences. Prior to joining the Jackson School, he spent 25 years in the petroleum industry where he worked as a research scientist (Mobil Oil and Phillips Petroleum) and research manager in (ConocoPhillips). His research interests include induced seismicity, structural geology, seismic structural analysis, reservoir geomechanics, and geology of West Texas and the Rocky Mountains. He is an AAPG distinguished lecturer, GSA fellow, and a founder of the AAPG Petroleum Structure and Geomechanics Division.

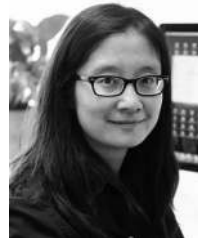


Katie Smye received a B.S. (2008) in geology and chemistry from the University of Oklahoma, and a Ph.D. (2013) in earth sciences from the University of Cambridge. She is a geoscientist working on subsurface characterization and integration in shale gas and tight oil basins and induced seismicity systems. She is the coprincipal investigator for the CISR at the BEG, UT Austin, and works with the tight oil resource assessment program. Her research interest includes the geologic characterization of producing formations and intervals used for disposal of flowback and produced water.



Scott Staniewicz received a B.S. (2013) in electrical engineering and mathematics from Tufts University, Medford, MA, USA, and an M.S. (2020) and Ph.D. (2022) in aerospace engineering from the University of Texas at Austin, Austin, TX, USA. He has been working at the Jet Propulsion Laboratory since 2022. His re-

search interests include large-scale InSAR processing and time-series analysis, statistical estimation, uncertainty quantification, and computer vision. He is a member of the American Geophysical Union and the IEEE.



Jingyi Chen received a B.S. (2008) in geophysics from the University of Science and Technology of China, Hefei, China, and an M.S. (2012) in electrical engineering and a Ph.D. (2014) in geophysics from Stanford University, California, USA. She has more than 10 years of experience in SAR/InSAR algorithm design for earth science applications,

and she is currently an assistant professor of Aerospace Engineering at the University of Texas at Austin. Her research interest includes the development of new satellite, and especially InSAR techniques for earth system science research. She is a member of the American Geophysical Union and IEEE.



Alexandros Savvaidis received a B.S. (1992) in geology, an M.S. (1997) in geophysics, and a Ph.D. (1998) in geophysics from Aristotle University of Thessaloniki, in Thessaloniki, Greece. He is the manager of the TexNet and seismology research team lead at the CISR at the BEG at UT Austin. He has more than 20 years of experience in applied geophysics and seismology. Prior to joining the BEG, he held the position of senior researcher at the Institute of Seismology and Earthquake Engineering in Thessaloniki, Greece. From 2008 to 2015, he was managing the largest seismographic network in Greece, numbering 100 real-time accelerometers and 150 offline installations. During his extensive career, he coordinated several collaborations with academic and industrial partners in multidisciplinary European-funded projects.